Changes in Atlantic Water circulation in the central Arctic Ocean between 2011 and 2021 inferred from tracer observations

Anne-Marie Wefing[1,2], Annabel Payne[1], Marcel Scheiwiller[1], Christof Vockenhuber[1,3], Marcus Christl[3], Toste Tanhua[4], and Núria Casacuberta[1,3]

[1]Department of Environmental Systems Science, ETHZ, Zurich, Switzerland
[2]Norwegian Polar Institute, Tromsø, Norway
[3]Laboratory of Ion Beam Physics, ETHZ, Zurich, Switzerland
[4]GEOMAR Helmholtz Centre for Ocean Research Kiel, Kiel, Germany

Correspondence: Anne-Marie Wefing (annemarie.wefing@npolar.no)

Abstract. ~~Atlantic Water circulation and associated changes play a crucial role in the future of the Arctic Ocean, especially in light of ongoing "Atlantification" trends. Still, the pathways, mixing properties, and circulation times of Atlantic Water in the Arctic Ocean remain to be better understood in view of recent variability and trends. Here, we~~ We use the long-lived anthropogenic radionuclides ~~I129 and U236 to investigate mixing between Atlantic and Pacific Waters in the surface layer and~~

5 ~~to determine Atlantic Water circulation times and mixing in the mid-depth Atlantic layer of the Arctic Ocean using the Transit Time Distribution (TTD) model. The~~ ^{129}I and ^{236}U to investigate Atlantic Water circulation in the central Arctic Ocean in 2021 and to assess temporal changes thereof between 2011 and 2021. This study is mainly based on radionuclide data ~~that has been~~ collected in the central Arctic Ocean during the "SAS-Oden 2021" expedition aboard the Swedish research icebreaker *Oden*, which was part of the Synoptic Arctic Survey (SAS) ~~programme. Furthermore, to assess temporal changes in the circulation~~

10 ~~pattern and circulation times of Atlantic Water between 2011 and 2021, we use available historic data on I129 and U236 between 2011 and 2021.~~ program. We use a mixing model to obtain tracer ages as well as the mixing of different endmembers in the surface layer. Atlantic Water circulation times and mixing in the mid-depth Atlantic layer are obtained from the Transit Time Distribution (TTD) model. For 2021, we find a sharp decrease in surface ~~I129 and U236~~ ^{129}I and ^{236}U concentrations between the Amundsen and Makarov Basins, pointing to significant fractions of Pacific Water reaching the Lomonosov Ridge

15 from the Amerasian side. In the halocline layer~~below, similar and comparably high I129 and U236 concentrations suggest a~~, similar ^{129}I and ^{236}U concentrations on both sides of the Lomonosov Ridge suggest a common formation region of halocline waters with a clear Atlantic Water signal in both the Amundsen and Makarov Basins close to the ridge. North of Greenland, we find a mixture of waters that originate from the Canada and Amundsen ~~basins~~Basins, both in the surface and the mid-depth layer. ~~The TTD model shows higher circulation times pointing~~Circulation times in the mid-depth layer point to a longer trans-

20 port route on the Makarov Basin side of the Lomonosov Ridge ~~. Regarding temporal changes, we~~ compared to the Amundsen Basin. Temporal changes in the circulation pattern and circulation times of Atlantic Water between 2011 and 2021 are obtained from available historic data on ^{129}I and ^{236}U between 2011 and 2021. We find a shift ~~in the location~~ of the Atlantic-Pacific Water front from ~~2011/12, when it was located further into~~ the Makarov Basin ~~,~~ towards the Lomonosov Ridge from 2011/12 to 2015 and 2021. In the mid-depth Atlantic layer, we observe an increase in mean and mode ages ~~show an increase~~ from

25 2015 to 2021, ~~which is in line with recent studies based on gas tracers and suggests~~ suggesting a slowdown or changes in the pathways of the Arctic Ocean Boundary Current, which is in line with recent studies based on gas tracers.

1 Introduction

1.1 A Changing Arctic Ocean~~circulation~~

30 The Arctic region is undergoing rapid changes as a result of anthropogenic climate change, including an unprecedented warming trend ~~with temperature increases that are four times higher than the global average (Rantanen et al., 2022). Especially relevant for the Eurasian Basin of the Arctic Ocean is the so-called "Atlantification", the~~ (Chapman and Walsh, 1993; Serreze et al., 2009; R , a decrease in sea-ice coverage and thickness (e.g., Kwok, 2018; Sumata et al., 2023), and changes in the ecosystem (e.g., Kohlbach et al., 2 . These changes are conveyed beyond the Arctic region, where they ultimately impact the global oceanic circulation. A

35 prominent example is the influence of a fresher Arctic outflow on dense water formation downstream, in the subpolar North Atlantic (e.g., Aagaard et al., 1985; Le Bras et al., 2021). A better understanding of the water mass composition and circulation patterns in the Arctic Ocean, as well as temporal changes thereof, is crucial to monitor ongoing changes and improve future projections.

40 Part of the observed changes in the Arctic Ocean are driven by the circulation of Atlantic-origin water, especially in the Eurasian Basin. Here, the expansion of warm Atlantic inflows into the Arctic, ~~contributing to the observed sea-ice decrease and weakening stratification(Polyakov et al., 2005, 2017). Recently, an increased oceanic heat flux from warm Atlantic Water at intermediate depths to the surface layer and sea ice has been observed, associated with~~ associated with weakening stratification, a thinned halocline layer~~(Polyakov et al., 2020). Wang et al. (2024) found the ongoing sea ice decline (e.g., Kwok, 2018) to act

45 as a primary driver of the atlantificationof the Eurasian Basin in the 2010s. Furthermore, the~~ , and enhanced vertical mixing, has been termed "atlantification" (Polyakov et al., 2005, 2017, 2020; Wang et al., 2024). The recent study by Polyakov et al. (2025) showed that this atlantification is not limited to the Eurasian Arctic anymore, but also observed beyond the Lomonosov Ridge, in the Makarov Basin.

50 ~~Atlantic Water enters the Arctic Ocean~~ Furthermore, temporal changes in the Arctic Ocean circulation are associated with shifts in atmospheric circulation patterns and coupled oceanic responses, described by indices such as the Arctic Oscillation (AO; e.g., Morison et al., 2012, 2021), the Arctic Ocean Oscillation (AOO; e.g., Proshutinsky et al., 2015), or the Arctic Dipole (AD; e.g., Polyakov et al., 2023). An increased AO index was for instance linked to an increase in the cyclonic atmospheric circulation of the Northern Hemisphere and a low Arctic sea level atmospheric pressure. It was therefore also termed the

55 "cyclonic mode" and found to induce shifts in freshwater pathways and in the front between Atlantic- and Pacific-derived waters in the surface layer of the central Arctic Ocean (Morison et al., 2012).

1.2 Arctic Ocean Circulation and Vertical Structure

In the cold and fresh surface layer of the Arctic Ocean, here referred to as Polar Surface Water (PSW), the two large-scale circulation patterns are the Beaufort Gyre and the Transpolar Drift. The Beaufort Gyre is an anticyclonic circulation system in the Canada Basin (e.g., Timmermans and Toole, 2023). The Transpolar Drift transports surface water and sea ice from the East Siberian Shelf and the Laptev Sea to the Fram Strait (e.g., Morison et al., 2012). Below the surface layer, warm and saline Atlantic-origin water forms the mid-depth Atlantic layer of the Arctic Ocean. Atlantic Water enters via two gateways, Fram Strait and the Barents Sea. Both branches are cooled along their northward passage and converge in the St. Anna Trough region. From here, the Fram Strait Branch Water (FSBW) and the Barents Sea Branch Water (BSBW) circulate cyclonically through the Arctic Ocean along different loops, forming the Arctic Ocean Boundary Current (AOBC). Part of the Atlantic Water recirculates to Fram Strait within the Eurasian Basin and part of it enters the Amerasian Basin, following a longer loop before also exiting through Fram Strait ~~. Pacific Water enters the Arctic Ocean through Bering Strait and is restricted to the upper layer due to its lower density compared to Atlantic Water and mainly resides in the Canada and Makarov basins (e.g., Rudels, 2015)~~ ~~(Fig. 1).~~(Fig. 1; e.g., Anderson and Jones, 1992; Schauer et al., 2002).

The ~~water column in the Arctic Ocean can be divided into different layers containing waters of different origin. The upper layer, here referred to as Polar Surface Water (PSW), is colder and fresher than the underlying warmer and more saline Atlantic Water. The PSW~~ PSW layer is highly stratified and generally entails Pacific Water, river runoff, sea-ice meltwater, as well as transformed Atlantic Water. ~~It~~ Pacific Water enters the Arctic Ocean through Bering Strait, mainly resides in the Canada and Makarov Basins, and is restricted to the PSW layer due to its low density (e.g., Coachman and Barnes, 1961; Rudels, 2015) (Fig. 1). PSW can be further divided into the Polar Mixed Layer (PML) at the surface, ~~defined by~~ reaching down to the temperature minimum~~that~~, which is a remnant of the previous winter convection ~~forming a deeper mixed layer (Korhonen et al., 2013)~~ (Rudels et al., 1996), and the halocline layer~~below~~. In the Eurasian Basin, the ~~transition between the PML and the deeper Atlantic Water with temperatures above 0°C is formed by the~~ halocline layer consists of the lower halocline (LHC). ~~The LHC~~, which originates from the cooling and freshening of Atlantic Water north of Fram Strait and the Barents Sea (Rudels et al., 1996; Korhonen et al., 2013). In the Amerasian Basin, the halocline ~~consists of~~ layer consists of the LHC and an additional layer ~~between the PML and the LHC~~above, the upper halocline (UHC). The UHC mainly consists of low salinity Pacific Water ~~inflow through Bering Strait~~ and Siberian river runoff ~~(Korhonen et al., 2013).~~ (Jones and Anderson, 1986; Anderson et al., 1994; Rudels et al., 20 . Below the PSW, Atlantic Water with temperatures above 0°C resides on top of intermediate and deep waters.

~~The Arctic Ocean plays a crucial role in the global oceanic circulation through the Atlantic Meridional Overturning Circulation (AMOC), and changes in Arctic circulation will therefore be conveyed beyond the Arctic region (e.g., Le Bras et al., 2021).~~
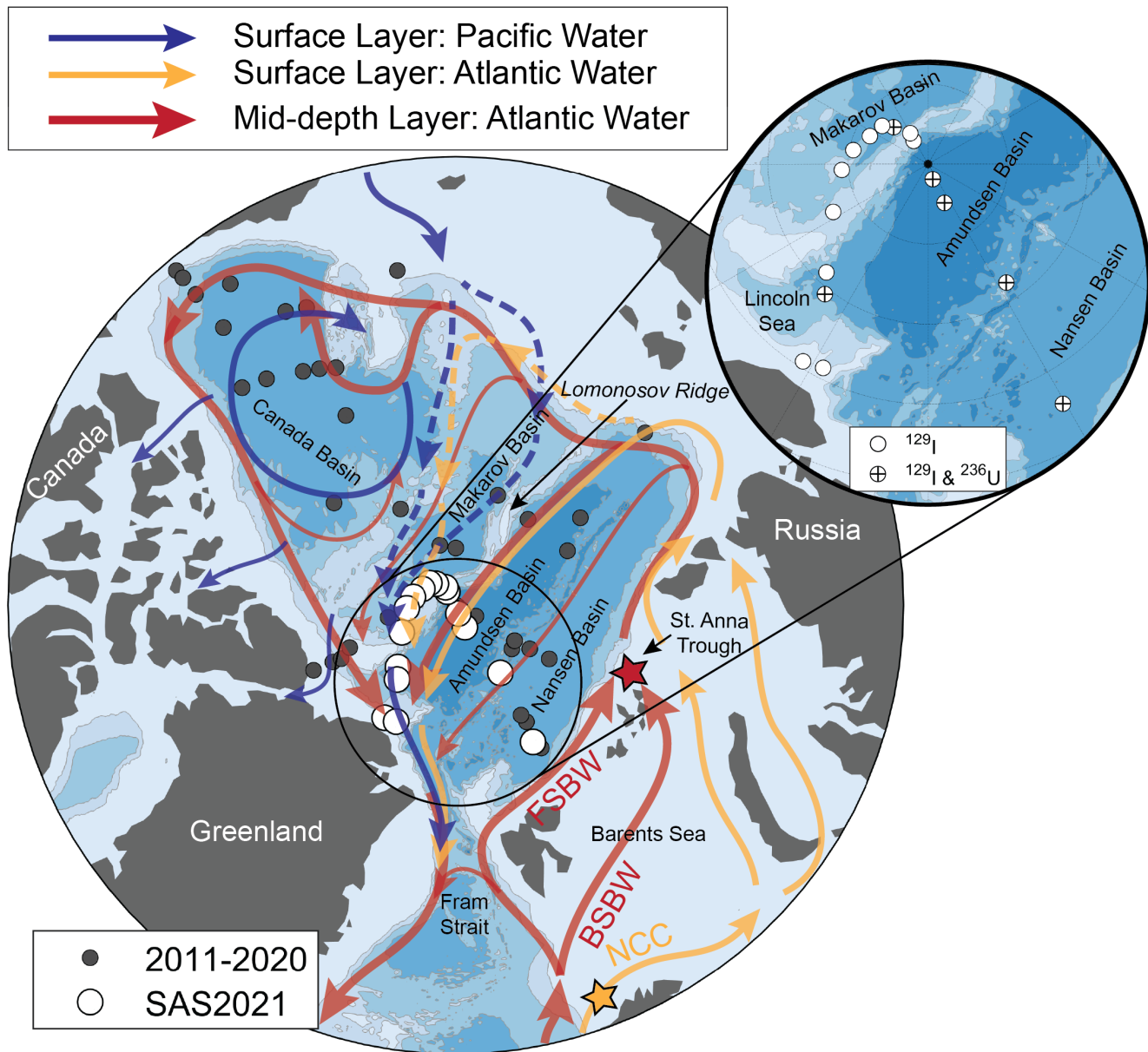
Figure 1. Map of the Arctic Ocean with main topographic and circulation features, as well as stations of radionuclide samples considered in this study. Blue and orange arrows show circulation patterns of Pacific (e.g., McLaughlin et al., 1996) and Atlantic Water (e.g., Rudels et al., 2004) in the surface, respectively, red arrows show circulation of Atlantic Water at mid-depth. FSBW: Fram Strait Branch Water, BSBW: Barents Sea Branch Water, NCC: Norwegian Coastal Current. The yellow and red star denote the locations where the surface layer input function (yellow, southern Barents Sea Opening) and mid-depth Atlantic layer input function (red, St. Anna Trough) were defined (see Fig. 2). Stations with published ^{129}I and ^{236}U data from earlier years (2011-2020) are shown in dark grey, see Section 2.1 for details. Radionuclide stations from SAS2021 are shown in white, with the inset further distinguishing stations where only ^{129}I data is available (white circles) and stations where ^{129}I and ^{236}U data is available (white circles with black cross).

1.3 Transient Tracers to study Atlantic Water Circulation in the Arctic Ocean

90 The role of Atlantic Water circulation in the Arctic Ocean and associated changes have been investigated through various methods, including modeling studies (e.g., Wang et al., 2024), extensive hydrographic measurements (e.g., Schulz et al., 2024), as well as tracer studies (e.g., Tanhua et al., 2009; Gerke et al., 2024; Körtke et al., 2024). As part of the latter, anthropogenic radionuclides labeling Atlantic Water have proven to be valuable tools (e.g., Smith et al., 2021; ?). In recent years, the two radionuclides I129 and U236 have been utilized as Atlantic Water tracers in several studies. The combination of I129 and

95 U236 provided a better understanding of Atlantic Water pathways (Casacuberta et al., 2018), Atlantic Water circulation times and changes therein (Wefing et al., 2021), mixing within the flow field (Payne et al., 2024), the uptake of anthropogenic carbon by Atlantic Waters (Raimondi et al., 2024), as well as mixing of different water masses and freshwater components in waters outflowing the Arctic through Fram Strait (Wefing et al., 2022). Here, we build on these works using the available historic I129 and U236 data from the Arctic Ocean together with new data collected in 2021, to investigate the distribution of different water

100 masses in 2021 and assess decadal changes in Atlantic Water circulation since 2011.

1.4 Anthropogenic radionuclides I129 and U236 as tracers of circulation changes

I129 and U236 are long-lived radionuclides with half-lives of about 16 Myr and 23 Myr, respectively. They have been introduced into the marine environment by two sources, both of anthropogenic origin. Firstly, liquid releases from nuclear reprocessing plants, which introduced mainly I129, and secondly, via global fallout from atmospheric nuclear weapon tests,

105 which introduced mainly U236 (Casacuberta et al., 2016). In the Arctic Ocean, releases from the two European reprocessing plants, Sellafield in the UK, and La Hague in France, are the dominant source of 129I and 236U, followed by the global fallout signal (only relevant for U236). The natural background of these two radionuclides is many orders of magnitude lower than the inputs from anthropogenic activities (Casacuberta et al., 2016).

The liquid releases of I129 and U236 from the two European reprocessing plants are transported northwards from the North

110 Sea to the Arctic Ocean mainly by the Norwegian Coastal Current (NCC) (Edmonds, 2001; Gascard et al., 2004; Smith et al., 2011; Christl . The global fallout signal is found in all water masses and introduced into the Arctic Ocean by both Atlantic and Pacific Water. The tracer signal carried by the NCC is also mixed into surrounding Atlantic Water during its northward passage, and hence all Atlantic Water entering the Arctic Ocean is tagged with a distinct tracer signature of I129 and U236 (Casacuberta et al., 2018, see also Secti . The concentration of I129 and U236 introduced by Pacific Water (global fallout signal) and its distribution in the Canada Basin

115 has been assessed in the recent study by Payne et al. (2024).

(e.g., Tanhua et al., 2009; Casacuberta and Smith, 2023; Gerke et al., 2024; Körtke et al., 2024). Classically, gas tracers such as CFCs and SF_6 have been used to study changes in Atlantic Water circulation, with a focus on ventilation timescales since this purpose (e.g., Broecker and Peng, 1982; Smethie et al., 2000). Since these tracers are introduced globally by air-sea gas exchange (e.g., Tanhua et al., 2009; Körtke et al., 2024), studies focused on ventilation timescales. The recent study by Gerke

120 et al. (2024) based on CFC-12 and SF_6 data from the Eurasian Basin collected between 1991 and 2021 found higher mean ages in the Amundsen Basin in 2021 compared to earlier years in the Amundsen Basin. This implies a decrease in ventilation,

which was found to have ~~happened~~ occurred primarily over the past 16 years~~and the~~. The authors speculate about a possible decrease in the strength of the ~~AOBC~~boundary current, increasing transport times of Atlantic Water. Körtke et al. (2024) investigated temporal changes in Atlantic Water pathways in the Arctic Ocean based on tracer ages obtained from CFC-12 and SF$_6$. Lower Atlantic Water tracer ages in the mid-1990s were attributed to a strong boundary current connected to a positive AO index (Morison et al., 2021, see also). Elevated tracer ages in 2005 and 2015 were interpreted as a weakening of the boundary current and coincided with phases of largely negative or mixed AO index. In addition, tracer age changes were also attributed to changes in the Atlantic Water pathways (see, e.g., Fig. 7 in Körtke et al., 2024).

~~In contrast to I129 and U236, CFCs and SF$_6$ have a global atmospheric source and can, therefore, be applied to investigate ventilation dynamics throughout the world's oceans. I129 and U236~~ Apart from gas tracers, anthropogenic radionuclides labeling Atlantic Water have proven to be valuable tools (Casacuberta and Smith, 2023). In recent years, the two radionuclides ^{129}I and ^{236}U, mainly introduced into the Arctic Ocean as liquid releases from European reprocessing plants, have been utilized as Atlantic Water tracers in several studies. The combination of ^{129}I and ^{236}U provided a better understanding of Atlantic Water pathways (Casacuberta et al., 2018), Atlantic Water circulation times and changes therein (Wefing et al., 2021; Smith et al., 2021), mixing within the flow field (Payne et al., 2024), the uptake of anthropogenic carbon by Atlantic Waters (Raimondi et al., 2024), as well as mixing of different water masses and freshwater components in waters outflowing the Arctic through Fram Strait (Wefing et al., 2022).

^{129}I and ^{236}U are most powerful in the Arctic Ocean and the subpolar North Atlantic, ~~but have the advantage that~~ downstream from the point-like input from the reprocessing plants. In contrast to CFCs and SF$_6$ they can also be used to asses circulation times in the surface layer, which is in contact with the atmosphere. For the comparison of gas tracers and radionuclides, the Arctic Ocean provides a unique configuration, since Atlantic Waters are isolated from atmospheric exchange once they subduct to depths and are capped by the halocline layer (see also Raimondi et al. (2024) for further discussion). With the rapid changes occurring in the Arctic Ocean, on the order of decades or below, available historical ~~I129 and U236~~ ^{129}I and ^{236}U data can now be used to assess temporal changes in Atlantic Water circulation (Smith et al., 2021), ~~to complement other tracer~~complementing tracer-based, hydrographic, and ~~model~~modeling studies.

~~In this study, we use I129 and U236 data collected in the central Arctic Ocean~~in 2021 to investigate Atlantic Water pathways, ~~mixing between Atlantic and Pacific Waters and other end-members in the surface layer, as well as Atlantic Water circulation times. We place~~ Here, we build on previous works using the available historic ^{129}I and ^{236}U data from the Arctic Ocean, together with new data collected in 2021. We use these tracers to investigate the distribution of different water masses in 2021, with a special focus on the Lincoln Sea north of Greenland, where waters from the Amerasian and Eurasian ~~basins~~ Basins converge before exiting the Arctic through the Nares or Fram Strait. Furthermore, we assess temporal changes in the circulation pattern and circulation times of Atlantic Water between 2011 and 2021. This study contributes to the understanding of how changes in

2 Material and Methods

2.1 Radionuclide Tracer Data

160 Seawater samples for the analysis of ~~I129 and U236~~ ^{129}I and ^{236}U were collected in 2021 during the "SAS-Oden 2021" expedition (SAS2021) aboard the Swedish research icebreaker *Oden* (Snoeijs-Leijonmalm et al., 2022), which was part of the Synoptic Arctic Survey (SAS). Hydrographic data from CTD profiles for this expedition is available on PANGAEA (Heuzé et al., 2022a). Biogeochemical bottle data is available both on PANGAEA (Heuzé et al., 2022b) and published in GLODAPv2.2023 (Lauvset et al., 2024). In total, 167 samples (16 full-depth stations) were taken for ~~I129~~ ^{129}I analysis and 48 samples (6 full-

165 depth stations) were taken for ~~U236~~ ^{236}U analysis at several stations along the cruise track from north of Svalbard towards the North Pole and further towards northern Greenland (Fig. 1). Samples were filled directly from the Niskin bottles mounted on the CTD-rosette into rinsed plastic 250 mL bottles (for ~~I129~~ ^{129}I analysis) and 3 L plastic cubitainers (for ~~U236~~ ^{236}U analysis) and shipped to ETH Zurich, Switzerland, for radionuclide analysis.

170 ~~I129~~ ^{129}I analysis followed the method of Casacuberta et al. (2016)~~, also described in Payne et al. (2024)~~. Samples were measured by Accelerator Mass Spectrometry (AMS) using the 0.5 MV AMS system *TANDY* at the Laboratory of Ion Beam Physics at ETH Zurich, Switzerland (Vockenhuber et al., 2015). Concentrated and diluted forms of an in-house standard, C2, were included with each measurement run (nominal value diluted: ~~129I~~ ^{129}I/~~127I~~ ^{127}I = 5.055×10^{-12} at at^{-1}, nominal value concentrated: ~~129I~~ ^{129}I/~~127I~~ ^{127}I = 38.995×10^{-12} at at^{-1}). All samples were corrected with chemistry blanks ($n = 12$) pre-

175 pared in the lab at ETH Zurich (MilliQ water, 18.2 MΩ). Relative uncertainties are largely around 3 %, based on the analytical uncertainty of the AMS measurement and repeated measurements of an ETH internal standard (standard deviation of 2 %, $n = 6$).

~~U236~~ ^{236}U analysis followed the method of Christl et al. (2015a)~~and has also been described in Payne et al. (2024)~~. Samples

180 were measured using the 0.3 MV AMS system *MILEA* at the Laboratory of Ion Beam Physics at ETH Zurich, Switzerland (Christl et al., 2023). Measured isotope ratios were normalized to the in-house standard ZUTRI (nominal values: 233U/~~238U~~ ^{238}U = $(33,170 \pm 830) \times 10^{-12}$ at at^{-1}, ~~236U~~ ^{236}U/~~238U~~ ^{238}U = $(4,055 \pm 200) \times 10^{-12}$ at at^{-1}) (Christl et al., 2013). ~~U236 and U238 concentration~~ ^{236}U and ^{238}U concentrations were calculated from the measured concentration of the U233 spike. All samples were corrected with chemistry blanks ($n = 5$) prepared in the lab at ETH Zurich (MilliQ water, 18.2 MΩ). Relative

185 uncertainties are largely around 3 %, based on the analytical uncertainty of the AMS measurement and assuming the same standard deviation of repeated measurements as for ~~I129~~ ^{129}I.

Table 1. Information on published radionuclide data from earlier expeditions used in this study.

Year	Cruise	Ship	Tracers	References
2011	PS78	RV Polarstern	~~I129, U236~~ ^{129}I, ^{236}U	Casacuberta et al. (2016); Wefing et al. (2021)
2012	PS80	RV Polarstern	~~I129, U236~~ ^{129}I, ^{236}U	Casacuberta et al. (2016); Wefing et al. (2021)
2012	Switchyard/LDEO	*aircraft*	~~I129~~ ^{129}I	~~Smith et al. (2021); ?~~ Smith et al. (2021); Casacuberta and Smith (20
2015	PS94	RV Polarstern	~~I129, U236~~ ^{129}I, ^{236}U	Casacuberta et al. (2018); Wefing et al. (2021); Raimondi et al. (202
2015	HLY1502	USCGC Healy	~~I129, U236~~ ^{129}I, ^{236}U	Smith et al. (2021); Chamizo et al. (2022); Raimondi et al. (2024)
2020	JOIS2020	CCGS Louis St Laurent	~~I129, U236~~ ^{129}I, ^{236}U	Payne et al. (2024)

~~I129 and U236~~ ^{129}I and ^{236}U data from SAS2021 are available on Zenodo (Wefing, 2025). To assess temporal changes over the past decade, we used published radionuclide data from several past expeditions to the Arctic Ocean ~~, which are listed in~~ (Table 1~~with references for corresponding radionuclide data~~).

2.2 ~~Tracer~~ Sources and Input Functions of ^{129}I and ^{236}U to the Arctic Ocean
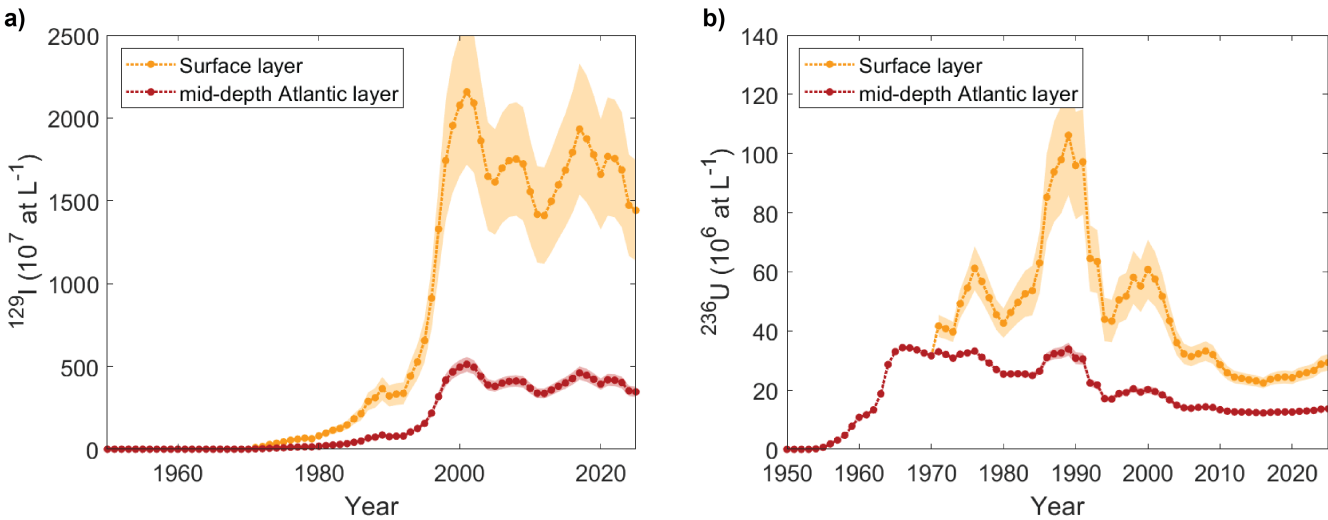

Figure 2. Input functions of ~~I129~~ ^{129}I (a) and ~~U236~~ ^{236}U (b) for the surface and mid-depth Atlantic layer, defined for the northern Norwegian Coast and the St. Anna Trough, respectively. Locations are marked with stars in Fig. 1. Shaded areas are the uncertainties of each input function.

^{129}I and ^{236}U are long-lived radionuclides with half-lives of about 16 Myr and 23 Myr, respectively, and negligible natural background concentrations in the marine environment (Casacuberta et al., 2016). They have been introduced into the ocean

by two anthropogenic sources. Firstly, liquid releases from nuclear reprocessing plants, which introduced mainly [129]I, and secondly, via global fallout from atmospheric nuclear weapon tests, which introduced mainly [236]U (Casacuberta et al., 2016). Although the nuclear weapon tests introduced significant amounts of [236]U (Sakaguchi et al., 2009), its global dispersion resulted in a low and relatively uniform background level that is now considered constant. In the Arctic Ocean, the dominant sources of [129]I and [236]U are therefore the liquid releases from the two European reprocessing plants, Sellafield in the UK, and La Hague in France.

The global fallout background signal (7×10^7 at L^{-1} for [129]I, Cooper et al. (2001), and 6.25×10^6 at L^{-1} for [236]U, Chamizo et al. (2022)) is found in all water masses and introduced into the Arctic Ocean by both Atlantic and Pacific Water. The reprocessing plant releases are transported northwards from the North Sea to the Arctic Ocean mainly by the Norwegian Coastal Current (NCC) (Edmonds, 2001; Gascard et al., 2004; Smith et al., 2011; Christl et al., 2015b, Fig 1). The tracer signal carried by the NCC is mixed into surrounding Atlantic Water during its northward passage, and hence all Atlantic Water entering the Arctic Ocean is tagged with a distinct tracer signature of [129]I and [236]U (Casacuberta et al., 2018).

Input functions of ~~I129 and U236~~ [129]I and [236]U describe the concentrations of both tracers entering the Arctic Ocean at a defined initialization point over time (Fig. 2). Here, we used the input functions defined and described in Wefing et al. (2021), which were also used in Raimondi et al. (2024) and Payne et al. (2024). Briefly, one input function for each radionuclide was defined for the surface layer, describing the concentrations of both tracers in Atlantic-origin Water that is transported with the ~~Norwegian Coastal Current~~ NCC over the shelf seas (Barents, Kara, and Laptev Sea) and enters into the Polar Surface Water. The initialization point for the surface layer input functions lies at around 72°N at the Barents Sea Opening, north of the Norwegian Coast (orange star in Fig. 1). A different input function for ~~I129 and U236~~ [129]I and [236]U was defined for the Atlantic layer, describing the concentrations of both tracers in Atlantic Water (FSBW and BSBW), forming the mid-depth Atlantic-origin layer of the Arctic Ocean. For the Atlantic layer input function, we consider the St. Anna Trough as the initialization point, since this is the location where FSBW and BSBW subduct and jointly form the Atlantic layer further downstream in the Arctic Ocean (red star in Fig. 1).

2.3 ~~Tracer ages and Transit Time Distributions~~Water Mass Classification

~~A Binary Mixing Model with I129 and U236~~ Water mass classifications used in this study followed the definition by Marnela et al. (2008) for the general water masses and (Korhonen et al., 2013) for the PSW (PML, UHC, LHC). Samples were generally divided into Polar Surface Water (PSW, $\sigma_\Theta < 27.70$) and Arctic Atlantic Water (AAW, $27.70 \leq \sigma_\Theta < 27.97$), as well as the intermediate ($27.97 \leq \sigma_\Theta, \sigma_{0.5} < 30.444$), and deep ($30.444 \leq \sigma_{0.5}$) layer. The PSW samples were further divided into the Polar Mixed Layer (PML, lower boundary defined by the temperature minimum) and the halocline layer. For samples from the Eurasian Basin, we only considered the lower halocline layer (LHC, from the lower boundary of the PML down to $\Theta = 0°$ C). For samples from the Amerasian Basin, we considered an additional upper halocline layer between PML and LHC

9

as described in Section 1.1 (UHC, from the lower boundary of the PML down to $S_p = 34$).

2.4 Tracer Ages and Dilution from Binary Mixing Model

For samples from PSW, a simple binary mixing model with ^{129}I and ^{236}U, assuming purely advective flow, was applied to determine radionuclide-based tracer ages and to investigate mixing between different end-members~~and to determine radionuclide-based tracer ages in PSW. Details are given in Wefing et al. (2021). Note that this is a simple model assuming purely advective flow~~. In this model, samples were plotted on top of mixing lines between the surface layer tracer input function and the steady-state global fallout signal in ^{236}U-^{129}I tracer space. Each binary mixing line reflects the dilution of the tracer signal carried into the Arctic Ocean by Atlantic Water in a specific year (described by the input function), with waters carrying the global fallout signal. The latter can either reflect a fraction of Atlantic Water not tagged with the reprocessing plants' tracer signal (Section 2.2) or Pacific Water that entered the Arctic Ocean through Bering Strait. Tracer ages of Atlantic Water (i.e., the time it took a water parcel to travel from the initialization point of the input function to the sampling location) were determined by finding the binary mixing line closest to the sample and correspond to the difference between sampling year and the input function year of that mixing line. Earlier studies have shown that this simple model yields reasonable results for circulation times in the surface layer of the Arctic Ocean (Smith et al., 2011; Casacuberta et al., 2018; Wefing et al., 2021).

For samples from the mid-depth Atlantic Layer and deeper, the binary mixing model was used solely to infer information on mixing and water mass provenance, as circulation times were obtained from the Transit Time Distribution (TTD) method.

2.5 Transit Time Distribution Model

The Transit Time Distribution (TTD) method was applied to describe the characteristics of Atlantic Water circulation in the mid-depth layer of the Arctic Ocean. This model has mainly been applied to ocean interior ventilation studies (e.g., Haine and Hall, 2002; Waugh et al., 2003; Tanhua et al., 2009; Stöven et al., 2015) and to determine anthropogenic CO_2 uptake by the ocean (e.g., Waugh et al., 2006; Khatiwala et al., 2013; Stöven and Tanhua, 2014; Stöven et al., 2016; Raimondi et al., 2024; Gerke et al., 2024). Its use with anthropogenic radionuclides has been investigated in several recent studies (Smith et al., 2011; Wefing et al., 2021; Smith et al., 2021) and the application to the ~~I129-U236 tracer pair have~~ ^{129}I-^{236}U tracer pair has been extensively described in Raimondi et al. (2024, therein referred to as "Smith's TTD approach"). Therefore, we will only provide a brief summary here.

In the TTD model, the concentration of a stable tracer at sampling location x and time t is described by

$$c(x,t) = \int_0^\infty c_0\left(t - t'\right) G\left(x, t'\right) dt' \tag{1}$$

where c_0 represents the tracer input function and $G(x,t)$ is the Green's function, which describes the propagation of the tracer signal and, therefore, the characteristics of the flow from the initialization of the input function to the sampling location. G is essentially a probability density function (PDF) reflecting the weight of tracer signals from different years of the input function at the specified sampling location and time. The flow is limited to 1D for simplicity, and in this case, the PDF is given by an inverse Gaussian function:

$$G(x,t) = \sqrt{\frac{\Gamma^3}{4\pi\Delta^2 t^3}} \; exp\left(-\frac{\Gamma(t-\Gamma)^2}{4\Delta^2 t}\right) \tag{2}$$

defined by two parameters, Γ and Δ. Γ represents the mean age of the distribution while Δ is a measure of the width of the PDF, and hence describes how much a tracer signal disperses during the flow as a result of lateral mixing. $\Delta = 0$ corresponds to purely advective flow. Another age measure of the distribution is the mode age t_{mode} (also termed most probable age, Smith et al., 2011; Wefing et al., 2021), the circulation time with the highest probability within the PDF. It is given by

$$t_{mode} = \frac{1}{\Gamma}\left(\sqrt{9\Delta^4 + \Gamma^4} - 3\Delta^2\right) \text{ with } t_{mode} \geq 1. \tag{3}$$

Previous studies suggested the mode age as a more suitable age measure for the lateral transport of Atlantic Water in the Arctic Ocean compared to the mean age (Smith et al., 2011; Wefing et al., 2021).

In the case of a mixture of two water masses with different transport histories that can each be described by a TTD, we consider considered a linear combination of two inverse Gaussian TTDs $G_1(\Gamma_1, \Delta_1)$ and $G_2(\Gamma_2, \Delta_2)$, each defining the flow field in the respective branch (Waugh et al., 2003; Smith et al., 2022):

$$G_{mix} = \alpha G_1(\Gamma_1, \Delta_1) + (1-\alpha)G_2(\Gamma_2, \Delta_2) \tag{4}$$

where α describes the fraction of the water mass described by $G_1(\Gamma_1, \Delta_1)$ in the mixture. The mean age of this bimodal TTD is a linear combination of the mean ages of G_1 and G_2. Δs do not mix conservatively, but are always higher in the mixture compared to a linear combination of the two end-members (see, e.g., Fig. 2b in Smith et al., 2022).

2.6 ~~Water mass classification~~

~~Water mass classifications used in this study followed the definition by Marnela et al. (2008) for the general water masses and (Korhonen et al., 2013) for the PSW (PML, UHC, LHC). Samples were generally divided into Polar Surface Water (PSW, $\sigma_\Theta < 27.70$) and Arctic Atlantic Water (AAW, $27.70 \leq \sigma_\Theta < 27.97$), as well as the intermediate ($27.97 \leq \sigma_\Theta, \sigma_{0.5} < 30.444$), and deep ($30.444 \leq \sigma_{0.5}$) layer. The PSW samples were further divided into the Polar Mixed Layer (PML, lower boundary defined by the temperature minimum that is a remnant of the previous winter convection forming a deeper mixed layer), and the halocline layer.For samples from the Eurasian Basin, we only considered the lower halocline layer (LHC, from lower boundary of the PML down to $\Theta = 0°$ C). For samples from the Amerasian Basin, we considered an additional upper halocline~~

11

In this study, the TTD method was applied to samples not classified as PSW and down to 1000 m. Deeper samples (1500 m and below) had ^{236}U concentrations close to the global fallout level or below (Fig. 3), and hence they did not carry significant amounts of the transient reprocessing plants tracer signal. The $\Delta - \Gamma$ grid for the determination of both TTD parameters according to "Smith's TTD approach" is shown in the appendix (Fig. A1).

3   Results

In the results section, we will first present the distribution of ^{129}I and ^{236}U from SAS2021 in depth profiles divided into two sections of the expedition (Fig. 3), along the SAS2021 transect as section plots of the upper 500 m (Fig. 4) and in relation to hydrographic parameters (Fig. 5). We restrict the latter to ^{129}I, due to the larger dataset compared to ^{236}U. We will then show tracer ages and dilution obtained from the binary mixing model for the PSW samples. Lastly, we will depict transport times and mixing from the TTD model for samples from the mid-depth Atlantic layer, as well as temporal changes in this layer.

3.1   Distribution of ^{129}I and ^{236}U

For all profiles from the Eurasian Basin section (Section 1), the highest ^{129}I concentrations were observed in the upper 100 m, with a peak in ^{129}I at 50-100 m for stations 25 and 26 (around 700×10^7 at L^{-1}, higher depth resolution for both stations compared to the other stations in section 1) and a peak at around 50 m for stations 16 and 20 (around 900×10^7 at L^{-1}) (Fig. 3a). At all stations, ^{129}I concentrations decreased with depth down to 500 m and increased again to a local maximum around 700 m (between 200×10^7 at L^{-1} and 400×10^7 at L^{-1}). Below 700 m, concentrations decreased further to almost 0 in the deepest samples at 3000 m depth. Generally, within the upper 1000 m, higher concentrations were observed at stations further north. Station 5 (located in the Nansen Basin) showed the lowest ^{129}I concentrations throughout the entire depth range (except for station 26 at 1000 m and below), especially in the upper 100 m. ^{129}I concentrations at Station 8 (at the Gakkel Ridge) were between those from station 5 and station 16. Station 26 (on top of the Lomonosov Ridge) showed the highest ^{129}I concentrations among all Section 1 stations between depths of 100 to 700 m, but concentrations decreased sharply between 700 and 1000 m. In contrast to ^{129}I, ^{236}U concentrations across Section 1 (sampled in lower spatial and depth resolution compared to ^{129}I) did not exhibit much variability in the upper 1000 m ($15 - 20 \times 10^6$ at L^{-1}) and no clear trend was observed among different stations (Fig. 3b). No apparent peak in ^{236}U concentrations was observed at 50-100 m, however, the sampling resolution was lower compared to ^{129}I. Similar to ^{129}I, a slight local maximum was observed at 700 m depth. ^{236}U concentrations reached global fallout
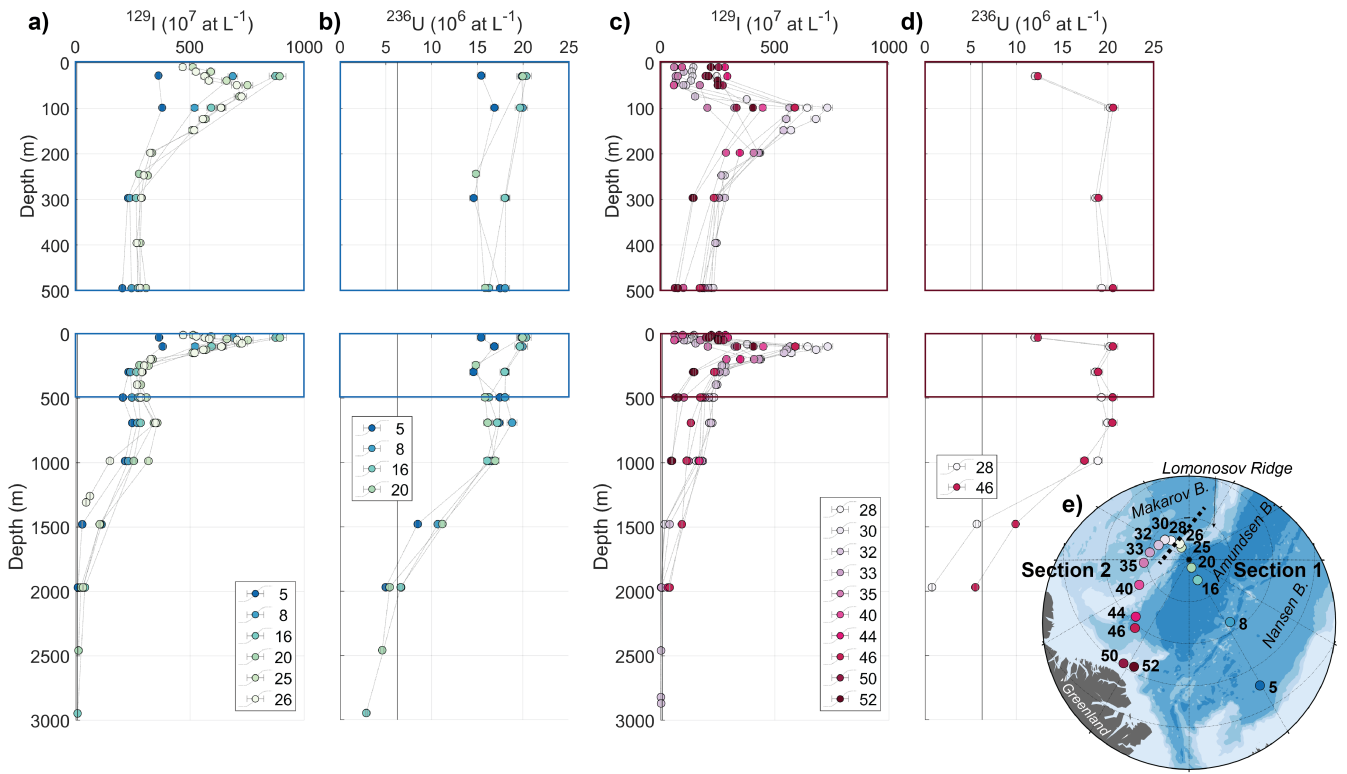
Figure 3. Depth profiles of ~~236U~~ ^{236}U and ~~129I~~ ^{129}I concentrations for all SAS2021 stations~~from~~, divided into two sections: Section 1 (a: ~~I129~~^{129}I, b: ~~U236~~^{236}U) comprises stations from the Nansen and Amundsen Basins up to the Lomonosov Ridge, Section 2 (c: ~~I129~~^{129}I, d: ~~U236~~^{236}U) comprises stations from the Makarov Basin and the region north of Greenland. Top row is a close up of 0-500 m, marked by the box in the full-depth profiles in the bottom row. Black vertical lines indicate global fallout background signal for both radionuclides from Payne et al. (2024)~~. Note that it~~, which is not distinguishable from zero in the ~~I29~~^{129}I profiles (panels a and c). (e) Map showing stations classified as Section 1 (blue-green colors) and 2 (red-purple colors). The dashed line indicates the division between both sections.

levels at around 2000 m depth and decreased further to around 3×10^6 at L^{-1} at 3000 m depth.

325   For the section through the Makarov Basin and north of Greenland (Section 2), the shape of ~~I29~~^{129}I profiles was different from ~~Section 1~~ the Eurasian Basin section in the upper 500 m. The maximum of ~~I29~~^{129}I concentrations ($200 - 700 \times 10^7$ at L^{-1}) was found around 100 m depth for all Section 2 stations, therefore, at greater depths than for Section 1 (Fig. 3c). Towards the surface, concentrations decreased to around $100 - 300 \times 10^7$ at L^{-1}. Surface ~~I29~~^{129}I concentrations of all Section 2 stations were lower than those from Section 1, and the overall lowest ~~I29~~^{129}I concentrations were observed for stations in the Makarov basin. Generally, as for Section 1, profiles further to the north exhibited higher concentrations (above 1000 m).

330   ~~U236~~^{236}U data was only analyzed for two stations from Section 2. Both profiles were very similar in the upper 1000 m (Fig. 3d). Above 100 m depth, ~~U236~~^{236}U concentrations decreased towards the surface, similar to ~~I29~~^{129}I, but in contrast,
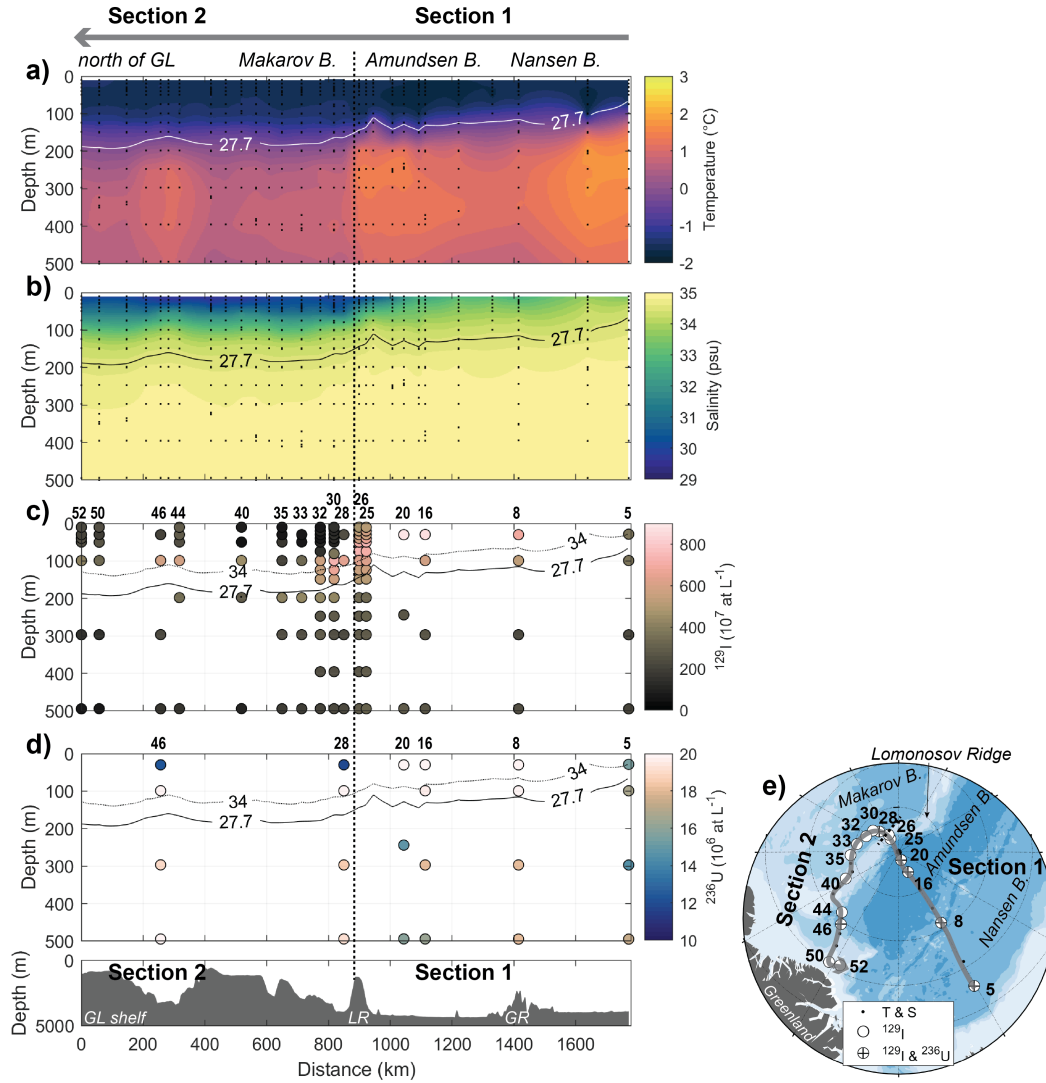
13

Figure 4. Section plots (upper 500 m) of CTD temperature (a), practical salinity (b), ~~I129~~ ^{129}I (c), and ~~U236~~ ^{236}U concentration (d), following the cruise track from the Nansen Basin (right-hand side of plots) to the Lomonosov Ridge (middle) and the Greenland shelf (left-hand side of plots). Continuous line is $\sigma_\Theta = 27.7$, dashed line in c and d is the isoline of practical salinity 34. Seafloor topography from GEBCO (GEBCO Compilation Group, 2024) is shown below the section plots, indicating the Greenland shelf (GL shelf), the Lomonosov Ridge (LR), and the Gakkel Ridge (GR). The transect is indicated as a grey line in the station map (e).

were almost constant over the depth range of 100-1000 m. Station 28 (in the Makarov Basin) showed a substantially lower ^{236}U concentration (almost 0) at 2000 m than all other stations (including those from Section 1).

At the Lomonosov Ridge (transition from Section 1 to Section 2, station 26 to 28, only ^{129}I data is available for both, brightest colors in Fig. 3), we observed a clear drop in ^{129}I from station 26 to 28, i.e., from the Amundsen Basin to the Makarov Basin, at depths of around 50 m (decrease of about 50 %) and between 500 and 1000 m (especially at 700 m, decrease of about 35 %). In contrast, between 50 and 500 m depth, concentrations were similar at both stations. Differences in upper layer ^{129}I and ^{236}U between Section 1 and Section 2 were also visible in the section plots covering both sections (Fig. 4). Above 100 m, the decline in ^{129}I and ^{236}U in Section 2 (left half of the section) was evident and coincided with a decrease in practical salinity from around 32.5 psu to around 30.5 psu at 50 m depth.

3.2 ^{129}I in Relation to Hydrographic Parameters

In the T-S plot (Fig. 5a, potential temperature against practical salinity, different water masses are highlighted following Section 2.3) the two sections of the expedition showed different features: PSW from Section 2 had slightly higher temperatures (difference around 0.5°C) compared to Section 1, for salinities above 32 (see also Section 4.2). In AAW and below, the opposite was observed, with Section 1 stations showing higher temperatures (difference up to 1°C) compared to Section 2 (Fig. 5b). Highest AAW temperatures of about 1.5°C (potential temperature) were observed at station 5 in the Nansen Basin, closest to the Atlantic Water inflow region. ^{129}I (color-coded) was high throughout the entire PSW in Section 1 and highest in the LHC for Section 2.

Different sampling regions showed different relations between ^{129}I and salinity (Fig. 5c). At practical salinities < 32 (PML), highest ^{129}I concentrations ($400 - 600 \times 10^7$ at L^{-1}) were found in samples from the Amundsen Basin (Section 1), followed by the stations north of Greenland (Section 2, $200 - 300 \times 10^7$ at L^{-1}). Makarov Basin stations (also Section 2) exhibited the lowest ^{129}I concentrations ($0 - 200 \times 10^7$ at L^{-1}) for salinities < 32. Within this salinity range, the two sections could not be clearly distinguished in T-S space, except for station 50, which showed higher temperatures at practical salinities between 30 and 31. In contrast, the three sampling regions of the Amundsen Basin (Section 1), the Makarov Basin (Section 2), and the stations north of Greenland (Section 2) differed significantly in ^{129}I, suggesting differences in the proportions of Atlantic-origin water carrying the tracer signal (see Section 3.1.1 for further discussion). In general, concentrations were more variable throughout the PML in Section 1, also within the same station (Fig. 5c). The PML in Section 1 extended to practical salinity 34 and

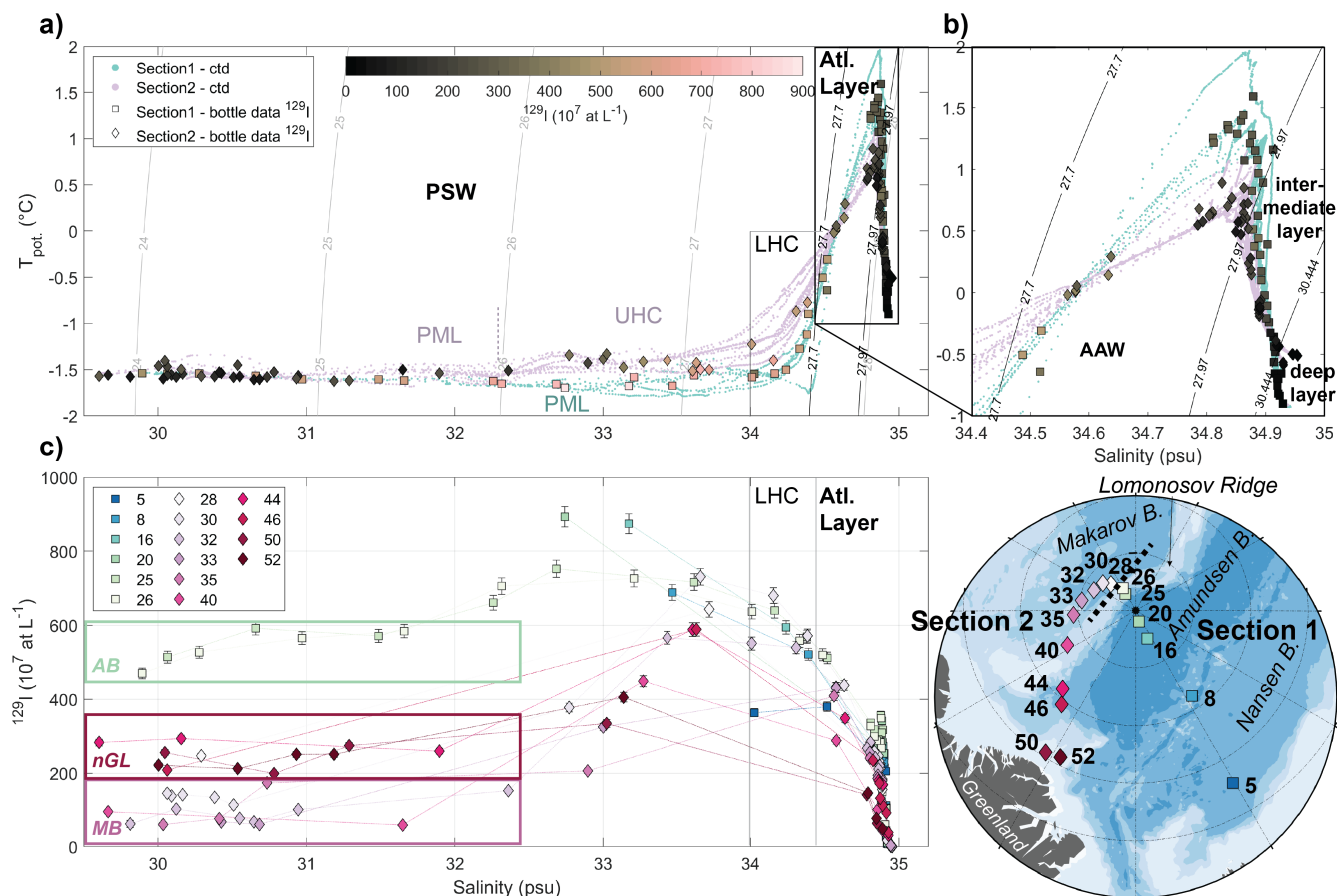**Figure 5.** (a) T-S plot (~~conservative~~ potential temperature against ~~absolute~~ practical salinity) with ~~I129~~ ^{129}I concentrations color-coded and different water masses indicated (PSW: Polar Surface Water, PML: Polar Mixed Layer, UHC: upper halocline, LHC: lower halocline, AAW: Arctic Atlantic Water). Teal and purple dots are 1 m-binned ~~ctd~~ CTD data from Section 1 and 2, respectively. Square and diamond data points are bottle file data from Section 1 and 2, respectively. (b) close-up of the Atlantic Layer (black box in a). (c) Plot of ~~I129~~ ^{129}I concentration against ~~absolute~~ practical salinity with stations color-coded. AB: Amundsen Basin, nGL: north of Greenland, MB: Makarov Basin.

there was no UHC layer, but we still observed a change in ~~I129 at a~~ ^{129}I at a practical salinity of around 32.5, approximately coinciding with the upper limit of the UHC layer in Section 2.

The highest ~~I129 concentrations~~ ^{129}I concentrations (around 900×10^7 at L^{-1}) of the entire SAS2021 dataset were found in ~~Amundsen Basin stations in the salinity range 32-34~~ the Amundsen Basin for practical salinities lower than 34, corresponding to the lower PML in Section 1 (Fig. 5c). For Section 2, the same salinity range corresponds to UHC waters and here, an increase in ~~I129~~ ^{129}I concentrations with increasing salinity was observed. The highest ~~I129~~ ^{129}I concentrations in Section 2 corresponded to the transition between UHC and LHC, ~~i.e., around a salinity of 34.~~ around a practical salinity of around 33.5. In contrast to the lower salinity range (PML), in the UHC layer (salinities between 32.5 and 34), samples from north of Greenland showed similar ~~I129~~ ^{129}I concentrations compared to those from the Makarov Basin. In the LHC (practical salinities > 34 but $\sigma_\Theta < 27.7$), the few available samples from the Amundsen (Section 1) and Makarov Basins (Section 2) had similar ~~I129~~ ^{129}I concentrations (no samples from the stations north of Greenland were available for ~~I129~~ ^{129}I in this salinity range). ~~Note the low I129~~ The low ^{129}I concentration of station 5 in the Nansen Basin ~~, likely reflecting~~ likely reflect the tracer concentration carried by inflowing FSBW ~~(see Section 3.1.1 for further explanation)~~(Wefing et al., 2021).

For samples from the Atlantic and intermediate layers close to the temperature maximum (~~salinities around 35~~practical salinities around 34.8), differences in ~~I129~~ ^{129}I between both sections of up to 200×10^7 at L^{-1} were observed (Fig. 5c). At similar salinities, samples from Section 1 showed higher ~~I129~~ ^{129}I concentrations, with a clear trend of decreasing ~~I129~~ ^{129}I from the Lomonosov Ridge (stations 25 and 26) towards the Nansen Basin (station 5, also observed in 3). ~~Also, among stations from~~ Along Section 2, the highest ~~I129~~ ^{129}I concentrations were found close to the Lomonosov Ridge (stations 28 and 30) and decreased towards the north of Greenland. ~~However, note the decrease in I129 in AAW at the~~ At the Lomonosov Ridge (between station 26 and 28~~,~~), ^{129}I in the AAW decreased from the Amundsen to the Makarov Basin~~)~~, which was also well observed in the profiles at depths between 500 and ~~100m~~1000 m (Fig. 3a and c). The lowest ~~I129~~ ^{129}I concentrations in AAW within Section 2 were found in Stations 50 and 52, close to Greenland. For ~~U236~~ ^{236}U (Fig. A2), a different trend between Section 1 and Section 2 was apparent. Here, in AAW and below, stations from Section 2 had higher ~~U236~~ ^{236}U concentrations compared to stations from Section 1 and the highest ~~U236~~ ^{236}U concentration was found in station 46. The distribution of ~~I129 and U236~~ ^{129}I and ^{236}U in the Atlantic Water layer will be further discussed in Section 3.1.1).

4 ~~Discussion~~

~~In the discussion, we will first highlight different aspects of the circulation of Atlantic Water in 2021 and then put these findings into the perspective of temporal changes based on previous tracer data (I129 and U236) collected across the Arctic Ocean since 2011.~~

3.1   Tracer Ages, Dilution, and Mixing of Atlantic Water~~Circulation in the Arctic Ocean in 2021~~

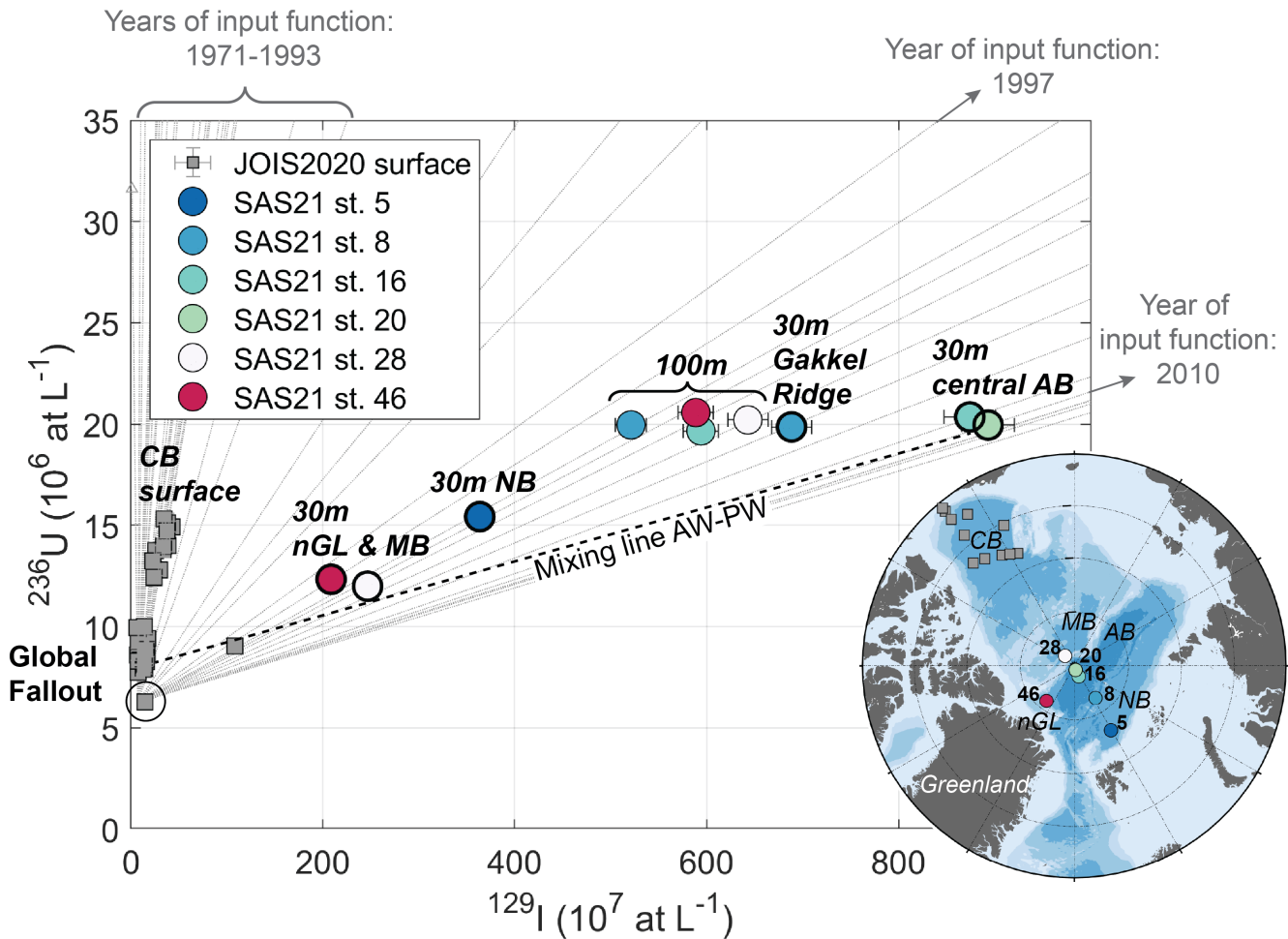### 3.1.1   ~~Circulation timescales in the surface layer~~

Figure 6. Plot of ~~U236~~ ^{236}U against ~~I129~~ ^{129}I concentrations with binary mixing lines (in grey) between individual years (1997-2010) of the surface layer input function (Fig. 2) and the global fallout background signal. SAS2021 PSW samples are color-coded by station. Thick black outline marks samples from around 30 m depth, thin black outline marks samples from around 100 m depth. CB: Canada Basin, nGL: north of Greenland, MB: Makarov Basin, NB: Nansen Basin, AB: Amundsen Basin. Samples from PSW in the Canada Basin collected in 2020 (JOIS2020, Payne et al., 2024) are shown in grey squares.

400 ~~Atlantic Water tracer ages and information on the dilution of the Atlantic Water tracer signal were obtained from a~~ In the binary mixing model~~in U236-I129 tracer space (Fig. 6, see also Casacuberta et al. (2018); Wefing et al. (2021); Dale et al. (2024)~~ ~~). Here, PSW samples are shown on top of mixing lines between the surface layer tracer input function and the steady-state~~

18

global fallout signal. Each mixing line reflects the dilution of the tracer signal carried into the Arctic Ocean by Atlantic Water in a specific year (described by the input function), with waters carrying only the global fallout signal (taken from Payne et al. (2024)). The latter can either reflect a fraction of Atlantic Water not tagged with the reprocessing plants' tracer signal (Section ??) or Pacific Water that entered the Arctic Ocean through Bering Strait. Tracer ages of Atlantic Water (i.e., the time it took a water parcel to travel from the initialization point of the input function to the sampling location) are determined by finding the binary mixing line closest to the sample and correspond to the difference between sampling year and input function year. Note that this is a simple model assuming purely advective flow of Atlantic Water and the presence of only two end-members in U236-I129 tracer space, but earlier studies have shown that it yields reasonable results for circulation times in the surface layer of the Arctic Ocean (Smith et al., 2011; Wefing et al., 2021).

In the dual-tracer plot, PSW samples from. , PSW samples from SAS2021 fell on binary plotted on mixing lines from years 1997 to 2010 of the surface layer input function with global fallout, translating to tracer ages of 11 to 24 years (Fig. 6). Shallow PSW samples from the Canada Basin (JOIS2020, grey squares in Fig. 6) are shown for comparison. They had much higher tracer ages (30-50 years) samples and the tracer signal was more diluted compared to the SAS2021 samples. Within SAS2021, shallow waters (around 30 m depth, thick black outline) from the central Amundsen Basin (stations 16 and 20) were the youngest (11-17 years). They showed the highest tracer concentrations, i.e., the least dilution with the global fallout signal. The shallow waters at station 8 (at the Gakkel Ridge) were slightly older (around 18 years) and more diluted compared to the central Amundsen Basin. The sample from a similar depth at station 5 in the Nansen Basin was older and more diluted than the Gakkel Ridge. Out of all PSW samples, those from the Makarov Basin and north of Greenland (stations 28 and 46) showed the highest dilution of the input function signal and the sample north of Greenland had the highest tracer age of about 23 years.

As pointed out above (Section 3.2) , station The four available data points from 100 m depth (thin black outline in Fig. 6) showed little variability in tracer concentrations, particularly in ^{236}U. Their tracer ages were around 18-22 years. The Eurasian Basin samples (station 8 and 16) displayed slightly more dilution of the input function signal compared to the shallower samples from the same stations, whereas the Makarov Basin and north of Greenland samples (station 28 and 46) were substantially less diluted than those from shallower depths.

In AAW, samples from the Makarov Basin and north of Greenland had lower ^{129}I concentrations paired with higher ^{236}U concentrations compared to samples from the Eurasian Basin (Fig. A). AAW samples from station 46 north of Greenland plotted on a mixing line between AAW from the Eurasian Basin and AAW from the Canada Basin (JOIS2020, Payne et al., 2024) . For AAW, no tracer ages were derived from the binary mixing model. Instead, transport times were obtained from the TTD model.

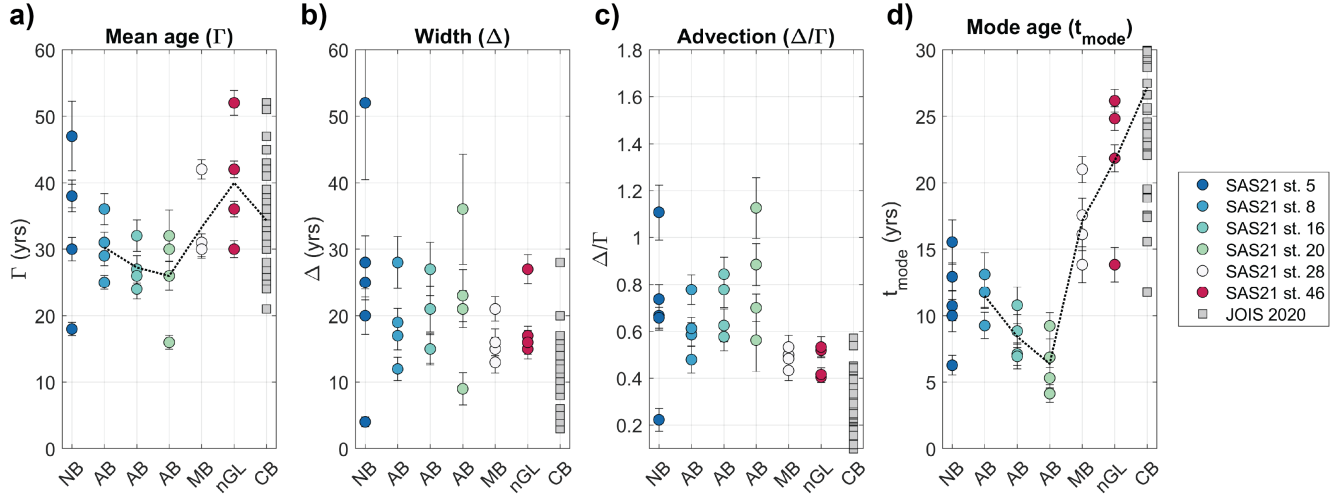## 3.2 Transport Times and Mixing in the Atlantic Layer from the TTD Model

Figure 7. TTD parameters Γ (mean age, a), Δ (width, b), derived Δ/Γ ratio (advection, c), and derived t_{mode} (mode age, d) plotted against different Arctic Basins for Atlantic layer samples from SAS2021 (down to 1000 m depth), color-coded by station. NB: Nansen Basin, AB: Amundsen Basin, MB: Makarov Basin, nGL: north of Greenland, CB: Canada Basin. Samples from the Atlantic layer in the Canada Basin collected in 2020 (JOIS2020, Payne et al., 2024) are shown in grey. Dashed lines in (a) and (d) connect mean values for each station.

The TTD parameters Γ and Δ, the Δ/Γ ratio, and the mode age t_{mode} derived for SAS21 and JOIS 2020 (Canada Basin) are presented in Fig. 7. For SAS2021, mean ages were overall in the range of 15-55 years, Δ largely between 9-40 years, Δ/Γ ratios were in the range of 0.4-1.2, and mode ages were below 30 years. Mean and mode ages both decreased from the Gakkel Ridge (station 8) towards the Lomonosov Ridge (station 20, Fig. 7a and d). From there, both ages increased towards the Makarov Basin and north of Greenland. Both trends were more pronounced in the mode age compared to the mean age, especially the abrupt change in the mode age when crossing the Lomonosov Ridge (from station 20 to 28). Δ/Γ ratios were generally higher in the Amundsen Basin (between 0.4 and 1.2) compared to the Makarov Basin and north of Greenland (both between 0.4 and 0.6). Δ/Γ ratios were lower in the Canada Basin than in all other basins. The Nansen Basin (station 5) showed a large spread in Γ and Δ.

Tracer concentrations north of Greenland pointed to a mixture of Atlantic Water coming from the Canada Basin and the Amundsen Basin (Fig. A). We assumed that Atlantic Water from each available sampling depth at station 46 can be described as a mixture of waters from similar depths at station PP7 in the ~~Nansen Basin had low tracer concentrations , both in I129 and U236, drawing it towards the global fallout end-member. This has been observed earlier (Wefing et al., 2021),~~ Canada Basin and station 20 in the Amundsen Basin (Fig. 8a). This was corroborated both by a T-S plot (Fig. 8b), as well as a ^{236}U-^{129}I plot (Fig. 8c), where dotted lines indicate linear mixing of CB and AB waters from respective depths. Samples from station 46 (dark red) plotted close to or directly on the mixing lines. Based on the mixing lines in ^{236}U-^{129}I tracer space, we calculated fractions of Amundsen Basin water found at each depth of station 46, and from those, the bimodal TTD from the individual
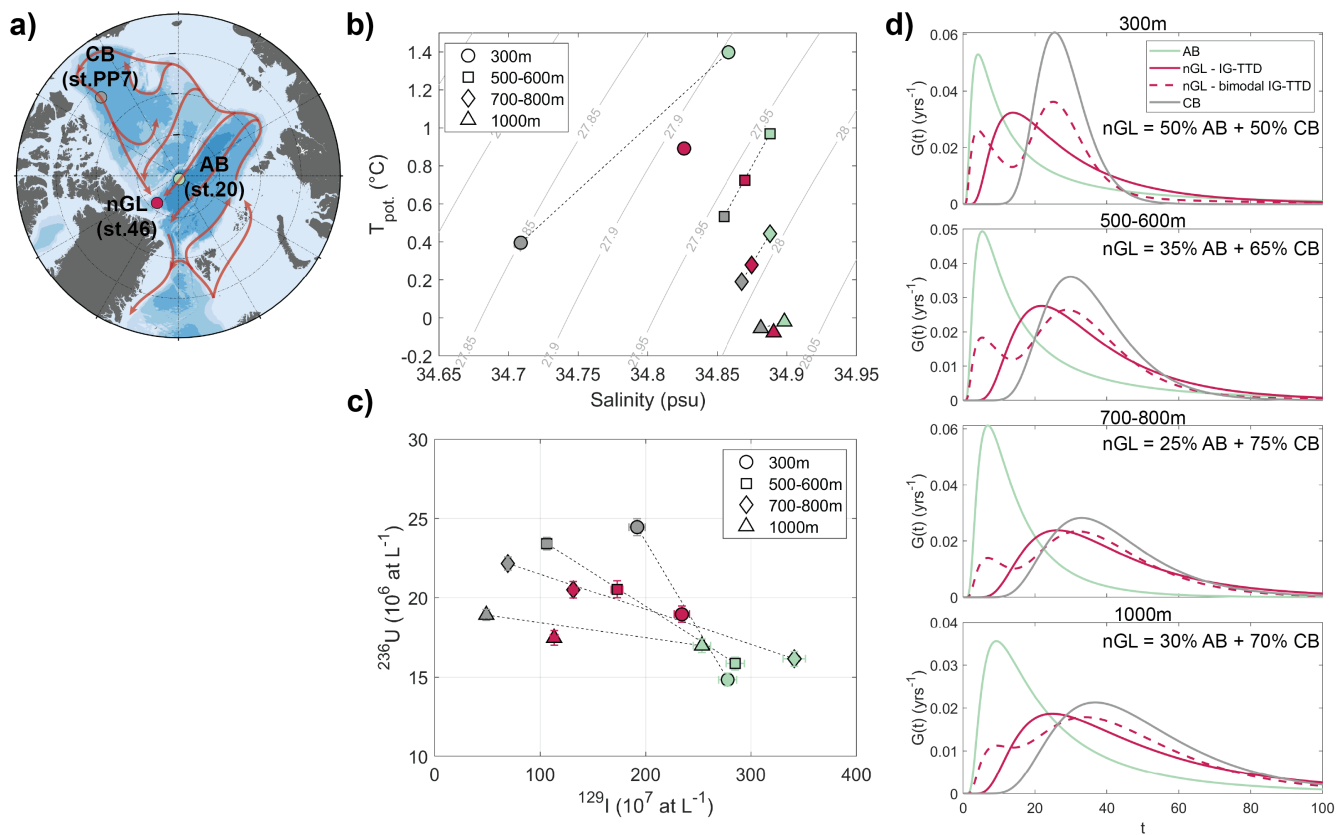
Figure 8. (a) Map showing station PP7 in the Canada Basin (CB, Payne et al. (2024)), station 20 in the Amundsen Basin (AB) and station 46 north of Greenland (nGL). Red arrows depict suggested Atlantic Water circulation, where station 46 is a mixture of waters from the other two stations. (b) T-S plot (potential temperature against practical salinity) of samples from available depths (300-1000 m, different symbols) from all three stations (color-coded). (c) ^{236}U-^{129}I plot of samples from available depths (different symbols) from all three stations (color-coded). (d) PDFs G(t) for available depths, color-coded by station. Dashed line depicts the bimodal IG-TTD for station 46.

TTDs of the end-members assuming a linear combination of two IG-TTDs (Eq. (4)).

455

The resulting bimodal PDFs for station 46 are shown in Fig. 8d (dark red, dashed), along with the unimodal PDFs of both end-members and station 46 (dark red, continuous). Compared to the PDFs from the Canada and Amundsen Basins (gray and green, respectively, in Fig. 8d), the unimodal PDFs at station 46 had a large width (large Δ) and hence a lower maximum probability, indicating the presence of more different ages within the distribution. Mean ages derived for station 46 from the bimodal TTD as a linear combination of the mean ages from the constituents were lower compared to those from the unimodal
460   TTD for all depths except 300 m. Furthermore, the bimodal PDFs decreased more rapidly towards old ages compared to the unimodal PDFs (Fig. 8d). In general, compared to the unimodal TTD for station 46, the Δ of the mixture was higher for the

upper two samples and lower for the others. When the flow field is described by a bimodal TTD, a single mode age cannot be attributed. Instead, the ages with the local maxima in the PDF describe the influence of the two end-members. At station 46, the overall highest probability in the PDF was associated with the Canada Basin branch for all depths.

3.3 Temporal Changes in Water Mass Circulation in the Atlantic Layer between 2011 and 2021
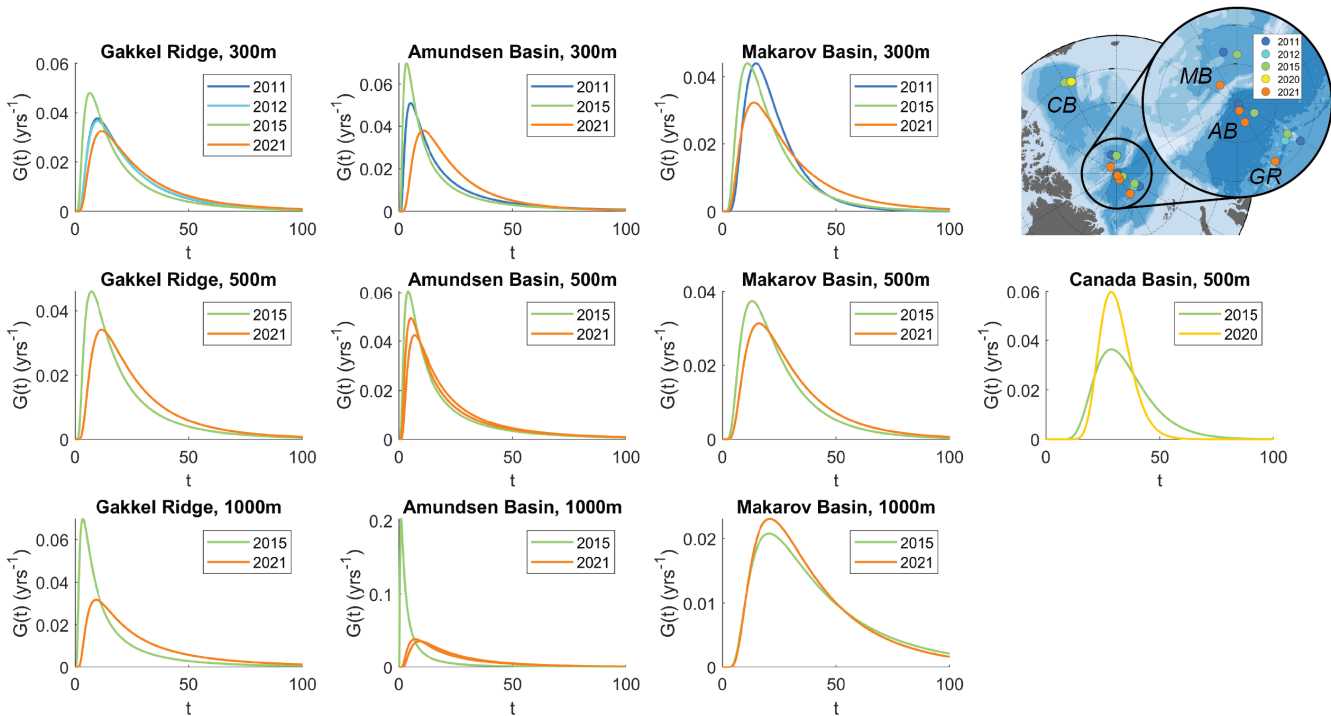

Figure 9. PDFs G(t) (different scales) for matching stations from different sampling years (2011 - 2021). Rows are different depths (300, 500, 1000 m), columns are different regions/basins. Stations and regions are shown on the map. GR: Gakkel Ridge, AB: Amundsen Basin, MB: Makarov Basin, CB: Canada Basin. TTD parameters can be found in Appendix C.

To assess temporal changes in Atlantic Water transport, we obtained the PDFs from the TTD model with [129]I and [236]U for available stations and depths within different Arctic regions, spanning the years 2011 to 2021 (Fig. 9, see Table 1 for details on available tracer data).

For the Eurasian Basin (stations at Gakkel Ridge and Amundsen Basin), the PDFs showed an increase of mean and mode ages over time, especially from 2015 to 2021. Δ did not show a clear trend and was largely similar in all years (Fig. A). These findings suggest an increase in the circulation time of Atlantic Water to the Amundsen Basin between 2015 and ~~since~~ ~~dilution with Pacific Water is not expected at the surface of Nansen Basin , it is most likely explained by northward-flowing~~

22

~~FSBW. This branch carries significantly lower concentrations of I129 and U236 compared to the surface layer input function (NCC, Casacuberta et al., 2018), which was confirmed again in the recent study by ?. Radionuclide concentrations in the Nansen Basin are not well described by the surface layer input function and are excluded from further interpretation.~~ 2021 that was not accompanied by an increase in mixing along the flow path. PDFs from the Makarov Basin showed a similar behavior between 2015 and 2021 down to 500 m depth. As for the Amundsen Basin, Δ remained largely unchanged over time. In contrast to the Amundsen Basin, mode ages in the Makarov Basin in 2015 and 2021 did not show a clear increasing trend. In the Canada Basin, samples from different years were only available at 500 m depth. While no change in the mode ages was observed, the shape of the PDF was altered due to a decrease in both Γ and Δ from 2015 to 2020 (Fig. A).

~~Note the~~

4   Discussion

4.1   Circulation Timescales in the Surface Layer

The surface layer circulation times obtained for Atlantic Water in 2021 are in line with the general circulation scheme (e.g., Rudels, 2015) and with findings from earlier studies based on the same tracers (Smith et al., 2011; Wefing et al., 2021; Casacuberta an . Young waters with a strong tracer signal found in the central Amundsen Basin suggest a more direct transport compared to the southern Eurasian Basin, potentially as part of the Transpolar Drift. In the Nansen Basin, lower tracer concentrations likely reflect the tracer concentration carried by inflowing FSBW, which is lower than that in the NCC (Casacuberta et al., 2018). The much higher tracer ages (30-50 years) and higher dilution of the tracer signal in PSW samples from the Canada Basin (JOIS2020, grey squares in Fig. 6) compared to the SAS2021 samples from the central Arctic ~~. This is~~ are due to the longer travel time of Atlantic Water to the Canada Basin and mainly Pacific Water being present at the surface ~~(see also Payne et al., 2024)~~ ~~.~~. North of Greenland, the higher tracer age compared to the Amundsen Basin suggests a mixture of Amundsen and Canada Basin waters.

4.1.1   ~~Pacific water extent~~

The estimates for lateral surface layer circulation times are particularly valuable since gas tracers do not provide reliable estimates due to their exchange with the atmosphere. Circulation times obtained from ^{129}I and ^{236}U depend on a well-constrained input function of both tracers. Future studies targeting the inflow region of Atlantic Water to the Arctic, such as the recent study by Pérez-Tribouillier et al. (2025), will help to improve our understanding of the Atlantic Water pathways. Especially in shelf seas such as the Kara and Laptev Seas, an improved quantification of freshwater input diluting the tracer signal will allow us to disentangle the water masses in the surface layer of the Arctic Ocean further.

4.2 ^{129}I as a Tracer for the Lateral Pacific Water Extent

~~Pacific water carries a low I129 and U236 tracer signal , corresponding to global fallout (latest estimate by Payne et al. (2024)).~~

510   Since ^{129}I is only carried into the Arctic Ocean by Atlantic-origin waters and Pacific Water dilutes the signal, the ^{129}I distribution across the SAS2021 study area can be used to asses the water mass composition in PSW. Here, we specifically address the lateral extent of Pacific Water, hence the front between Atlantic- and Pacific-derived waters. In order to assess the presence of Pacific water in the study area based on the tracer ~~distribution~~concentrations, however, other tracer-free water masses have to be considered, here meteoric water (~~mainly river water~~net precipitation and river runoff) and sea-ice meltwater.

515

     The overall decrease ~~of I129 (and U236~~in ^{129}I (and ^{236}U) with decreasing salinity throughout the PML in Section 1 (Fig. 5c and Fig A2) points to a dilution of the tracer signal with low-salinity ~~water. The~~ waters. A combination of salinity, stable oxygen isotopes (δ^{18}O), and nutrient ratios (Nitrate to Phosphate, referred to as the N:P ~~fractions~~method) was used to calculate mete-oric, sea-ice meltwater, Atlantic and Pacific Water fractions ~~(e.g., Östlund and Hut, 1984; Bauch et al., 2011; Paffrath et al., 2021)~~

520   (e.g., Östlund and Hut, 1984; Jones et al., 1998; Bauch et al., 1995, 2011; Paffrath et al., 2021), here using end-member values from Bauch et al. (2011) and following the calculations outlined therein (Fig. A5a-c). Meteoric water fractions were up to ~~1~~0.12, highest in the upper 50 ~~(highest at the surface)~~m in the Amundsen and Makarov Basins. In contrast, sea-ice meltwater fractions were mostly negative (between ~~-4~~-0.04 and 0~~-~~), pointing to brine rejection and net sea-ice formation, and were highest for the stations north of Greenland (up to ~~2~~0.02).

525

     ~~Assuming negligible to no I129 input by meteoric water (Casacuberta et al., 2016), I129 concentrations were~~ ^{129}I concentrations were then corrected to 100 % saline water by the calculated meteoric water fractions, assuming negligible to no ^{129}I input by meteoric water (Casacuberta et al., 2016) (Fig. A5d~~,~~). The small and largely negative sea-ice ~~melt was omitted since it was largely negative or around zero). Also, after~~meltwater fractions were omitted. After correcting for the meteoric water frac-

530 tion, we still observed a decrease in ~~I129~~^{129}I towards the surface, ~~which showed~~ showing that dilution with meteoric water only explains part of the decrease in ~~I129~~^{129}I towards low salinities. Dilution with older Atlantic Water (carrying lower ^{129}I concentrations, see Fig. 2a) cannot explain the decrease in ^{129}I concentrations, as this would be accompanied by an increase in ^{236}U (Fig. 2b). Therefore, dilution with Pacific Water most likely explains the decrease of ~~I129~~^{129}I concentrations towards the surface.

535

     Pacific Water fractions ~~obtained from N:P ratiosare debated and have~~ have been estimated using various parameters (e.g., silicate, nutrient ratios, gallium), each with its strengths and limitations. These methods remain debated and carry large un-certainties (e.g., Alkire et al., 2015, 2019; Whitmore et al., 2020), however, they still serve for an overview of the spatial distribution of Pacific Waters across the sampling area. For the SAS2021 samples, N:~~P based~~P-based Pacific Water fractions

540 ~~suggest~~ suggested that Pacific Water was present in all PSW samples, with ~~highest fractions~~the highest fractions of 0.8-1

found in the Makarov Basin (Fig. A5c), supporting the hypothesis of tracer dilution by Pacific Water at all stations. This ~~is was~~ also corroborated by the dual-tracer plot (Fig. 6), where samples from north of Greenland and the Makarov Basin fell on a mixing line between the central Amundsen Basin samples to Canada Basin surface samples close to global fallout. ~~Note that from~~ From the N:P ~~ratio~~ method, we obtained similar Pacific Water fractions for PSW in the Amundsen Basin and north

545 of Greenland. At the same time, ~~I129 concentrations are~~ ^{129}I concentrations were significantly different between ~~both~~ the two regions. This might be caused by an overestimation of the N:P-based Pacific Water fractions for the Amundsen Basin (Alkire et al., 2015; Bauch et al., 2011; Newton et al., 2013), similar to the findings of Alkire et al. (2019)~~who~~. They reported a larger extent of Pacific Water towards the Eurasian Basin based on the N:P ~~ratios compared to the NO parameter~~method compared to other methods and suggested uncertainties of 40 % or more associated with N:P-based Pacific Water fractions.

550

Generally, based on the combined ~~I129 and U236~~ ^{129}I and ^{236}U data, we can hence conclude that the front between Atlantic and Pacific-derived waters in the surface layer of the central Arctic was located somewhere between station 20 and station 28 in 2021, due to the different location of surface samples from these two stations in the ~~U236-I129~~ ^{236}U-^{129}I mixing plot (Fig. 6). With the better spatial resolution for ~~I129~~^{129}I, and the sharp decrease in surface ~~I129~~^{129}I concentration between station 26 (on

555 top of the Lomonosov Ridge) and station 28 (Makarov Basin) (Fig. 3 and Fig. 5), we can restrict it further to the Makarov Basin side of the Lomonosov Ridge. However, the presence of some Pacific Water is required to explain the ~~decrease in I129 in~~ lower ^{129}I concentrations in the surface waters of stations 25 and 26 compared to station 20, which is supported by the N:P ~~ratios~~method.

560 **4.2.1** ~~**Provenance of Halocline Waters**~~

~~For the halocline layer, combined I129 and U236 data was available for four stations, two in the Amundsen Basin, one in the Makarov Basin, and one north of Greenland (Fig. 5 and 6, data points from 100 depth with thin black outline). These data points all plotted at a similar location in the mixing plot, and especially U236 concentrations were strikingly consistent among them. Note that these samples also had the highest I129 concentrations throughout the water column in the Makarov Basin and~~
565 ~~north of Greenland (Fig. 3).~~

~~Based on their T and S properties, the two samples from the Amundsen Basin (station 8 and 16) were associated with the LHC, which is formed north of the Barents Sea from cooled and freshened Atlantic Water carried in Fram Strait and Barents Sea Branch Water, and through the addition of low-salinity shelf water mainly from the Laptev Sea (Rudels et al., 1996). The samples from the Makarov Basin (station 28) and north of Greenland (station 46) had practical salinities slightly~~
570 ~~below 34. They were, therefore, classified as UHC waters by hydrographic properties and are thought to be derived from Pacific inflow but also influenced by the East Siberian Sea (e.g., Anderson et al., 2017). However, this is not supported by the radionuclide concentrations. The similar location of the 100 samples from the different stations in the dual-tracer plot suggests a common origin or formation region and transport route for these halocline waters, before they are transported across the Arctic Ocean towards Greenland. This is also supported by the additional available I129 data, where samples from~~

the Amundsen and Makarov Basins showed similar I129 concentrations throughout the LHC layer (Fig. 5c and Fig. **??**a). Furthermore, the comparably high tracer concentrations suggest only little Pacific-origin water but a significant fraction of tracer-labeled NCC-origin waters, which are transported along the Eurasian shelf and contribute to the formation of halocline waters along their way. Based on the I129 and U236 concentrations presented in this study, we conclude that halocline waters formed from Atlantic-origin waters are present throughout the entire study area, including the Makarov Basin and the area north of Greenland. This is also supported by the distribution of the NO parameter at a practical salinity of 34 (NO = (9×NO$_3^-$) + O$_2$, Broecker (1974), Fig. **??**b), which does not show a lot of variation across the study area. NO values are below 400 which was used by Alkire et al. (2019) to discriminate Atlantic from Pacific waters.

4.2.1 Transport Times and Mixing in the Atlantic Layer

For samples from the mid-depth Atlantic Layer and below, For a better assessment of the dual-tracer method was only used to infer information on mixing and water mass provenance, since circulation times were obtained from the TTD approach. Lower I129 concentrations, paired with higher U236 concentrations observed in Section 2 compared to Section 1, (Fig. A) indicate the influence of water from the Canada Basin. AAW samples from Section 2, especially from station 46 north of Greenland, plotted on a mixing line between AAW from Section 1 and AAW from the Canada Basin (JOIS2020, Payne et al., 2024). This suggests that AAW north of Greenland represents a mixture of Atlantic Water that has circulated through the "long loop" (Canada Basin) and the "short loop" (Eurasian Basin), which will be investigated further under the framework of the TTD model.

The TTD method was applied to samples not classified as PSW and down to 1000 . Deeper samples (1500 and below) showed U236 concentrations close to the global fallout level or below (Fig. 3), and hence they did not carry significant amounts of the transient reprocessing plants tracer signal. The $\Delta - \Gamma$ grid for the determination of both TTD parameters according to "Smith's method" (see Raimondi et al. (2024) for detailed explanation) is shown in the appendix (Fig. **??**).

TTD parameters Γ (mean age, a), Δ (b), derived Δ/Γ ratio (c), and derived t_{mode} (mode age, d) plotted against different Arctic Basins for Atlantic layer samples from SAS2021 (down to 1000 depth), color-coded by station. NB: Nansen Basin, AB: Amundsen Basin, MB: Makarov Basin, nGL: north of Greenland, CB: Canada Basin. Samples from the Atlantic layer in the Canada Basin collected in 2020 (JOIS2020, Payne et al., 2024) are shown in grey. Dashed lines in (a) and (d) connect mean values for each station.

The two parameters of the TTD obtained for the SAS21 samples and the Canada Basin 2020 position of the Atlantic-Pacific-Water front, an increased spatial sampling resolution of at least [129]I would be preferable. With the available data, Γ and Δ, as well as the derived parameters Δ/Γ and the mode age t_{mode}, are plotted in Fig. 7. Different stations from SAS2021 are color-coded and sorted by basin. For SAS2021, mean ages were overall in the range of 15-55 years, Δ largely between 9-40 years, Δ/Γ ratios were in the range of 0.4-1.2, and mode ages were below 30 years. Δ/Γ ratios were generally higher in the Amundsen Basin (between 0.4 and 1.2) compared to the Makarov Basin and north of Greenland (both between 0.4 and 0.6). Confirming previous studies (Wefing et al., 2021; Raimondi et al., 2024), Δ/Γ ratios were lower in the Canada Basin than in all other basins. Note the large spread in Γ and Δ for the Nansen basin (station 5). Since this station is not

located downstream of the initialization point of the Atlantic Layer input function (the St. Anna Trough, where FSBW and BSBW merge), the TTD analysis is not expected to provide meaningful results. This was already shown in earlier studies (Wefing et al., 2021; Raimondi et al., 2024; ?) and we will not include the samples from station 5 in the further interpretation.

Mean and mode ages both decreased from the Gakkel Ridge (station 8) towards the Lomonosov Ridge (station 20, Fig. 7a and d). From there, both ages increased towards the Makarov Basin and north of Greenland. Both trends were more pronounced in the mode age compared to the mean age, especially the abrupt change in the mode age when crossing the Lomonosov Ridge (from station 20 to 28). Previous studies suggested the mode age as a more suitable age measure for the lateral transport of Atlantic Water in the Arctic Ocean compared to the mean age (Smith et al., 2011; Wefing et al., 2021). The decrease in mode ages from the central Eurasian Basin towards the Lomonosov Ridge suggests that waters in the mid-depth Atlantic layer are transported faster close to the ridge, which could be explained by transport in a branch of the Arctic Ocean Boundary Current flowing along the Amundsen Basin side of the Lomonosov Ridge. The same spatial pattern was observed by Körtke et al. (2024), investigating tracer ages from CFC-12 and SF_6, as well as Pasqualini et al. (2024), from ^{3}H-^{3}He ages. However, interestingly, Δ/Γ ratios do not suggest very advective transport at station 20, but rather increase from the interior Eurasian Basin towards the Lomonosov Ridge, pointing to more mixing along the flow. In the Makarov Basin, north of Greenland, and in the Canada Basin, low Δ/Γ ratios and high mode ages point to more advective flow, but a longer pathway of waters. The significantly higher mode ages in the Makarov Basin suggest that waters have been transported along a different (longer) loop compared to the Amundsen Basin. A difference in water mass ages between both sides of the Lomonosov Ridge was also observed by Tanhua et al. (2009) and Gerke et al. (2024), albeit in mean ages derived from gas tracers. Both studies found higher mean ages, i.e., a slower ventilation, in the Makarov Basin compared to the Amundsen Basin, with a sharp front over we can constrain the position across the sampled transect, but not in other regions across the Arctic Ocean. It cannot be concluded from this dataset whether the front was generally aligned with the Lomonosov Ridge . This is in line with our findings based on I129 and U236, confirming that anthropogenic radionuclides and gas tracers such as CFCs and SF_6 act as similar Atlantic Water tracers in the Arctic Ocean once the Atlantic Water layer is isolated from atmospheric gas exchange. This has also been discussed in Raimondi et al. (2024), with implications for anthropogenic carbon estimates from I129 and U236. or only happened to be at the ridge at the sampled stations.

(a) Map showing station PP7 in the Canada Basin (CB), 20 in the Amundsen Basin (AB) and 46 north of Greenland (nGL). Red arrows depict suggested Atlantic Water circulation, where station 46 is a mixture of waters from the other two stations. (b) T-S plot (conservative temperature against absolute salinity) of samples from available depths (300-1000 , different symbols) from all three stations (color-coded). (c) U236-I129 plot of samples from available depths (different symbols) from all three stations (color-coded). (d) PDFs G(t) for available depths, color-coded by station. Dashed line depicts the bimodal IG-TTD for station 46.

As mentioned above, tracer concentrations at station 46, located north of Greenland, pointed to a mixture of Atlantic Water coming from the Canada Basin and the Amundsen Basin. This is also reflected in the PDFs constructed for the available samples from this station. Compared to the PDFs from the Canada and Amundsen Basins, PDFs at station 46 had a large

width (large Δ) and hence a lower maximum probability, indicating the presence of more different ages within the distribution.
In fact, the mixture of two branches with a different transport history is not captured by the TTD model using a unimodal inverse Gaussian function. Instead, Smith et al. (2022) described the linear combination of two inverse Gaussian functions, each defining the flow field in the respective branch. We assumed that Atlantic Water from each available sampling depth at station 46 can be described as a mixture of waters from similar depth at station PP7 in the Canada Basin (Fig. 8a and Payne et al. (2024)) and station 20 in the Amundsen Basin. This is corroborated both by a T-S plot (Fig. 8b), as well as a U236-I129 plot (Fig. 8c), where dotted lines indicate linear mixing of CB and AB waters from respective depths. Note how samples from station 46 (dark red) plotted close to or directly on the mixing lines even though the sampling depths/potential density of the available samples did not match exactly. Based on the mixing lines in U236-I129 tracer space, we calculated fractions of Amundsen Basin water found at each depth of station 46, and from those, the bimodal IG-TTD from the individual TTDs of the end-members assuming a linear combination of two IG-TTDs (see equation 4).The resulting bimodal TTDs for station 46 are shown in Fig. 8d (dark red, dashed), along with the unimodal IG-TTDs of both end-members and station 46 (dark red, continuous). The mean age of the bimodal TTDs is a linear combination of the mean ages of both end-members. Mean ages derived for station 46 from the bimodal TTD were lower compared to those from the unimodal TTD for all depths except 300 . This result is more reasonable given that the unimodal mean ages were on the order of or even exceeding those from the Canada Basin (see also Fig. 7a). The effect is also seen in the more rapid decrease of the bimodal TTD at old ages (Fig. 8d). Δs do not mix conservatively, but are always higher in the mixture compared to a linear combination of the two end-members (see, e.g., Fig. 2b in Smith et al., 2022). For the sample from around 700 depth, the Δ corresponding to the bimodal TTD even exceeded the individual Δs of the end-members. In general, however, compared to the unimodal TTD for station 46, the Δ of the mixture was higher for the upper two samples and lower for the others. When the flow field is described by a bimodal TTD, a single mode age cannot be attributed. Instead, the ages with the local maxima in the PDF describe the influence of the two end-members. Note that for station 46, the overall highest probability in the PDF was associated with the Canada Basin branch for all depths. Overall, we conclude that the Atlantic Water transport north of Greenland should rather be described by a bimodal TTD than a unimodal one, considering the two branches of Atlantic Water being advected from the Amundsen and Canada Basins. This applies to other regions of the Arctic Ocean as well, such as the mixing of Atlantic and Pacific-derived water over the Chukchi Sea shelf described in Smith et al. (2022).

4.3 Temporal changes Changes in Atlantic the Pacific Water circulation between 2011 and 2021Extent

4.3.1 Changes in Polar Surface Water

To assess temporal changes in Polar Surface Waters, we compared available I129 The compilation of available ^{129}I data collected in the Eurasian and Makarov Basin Basins between 2011 and 2021 (see Table 1) . The distribution of I129 concentrations in the surface (around was used to assess temporal changes in the lateral extent of Pacific Water. The ^{129}I distribution in surface waters (approximately 10-30 mdepth , depending on sample availability) showed the overall pattern of a higher I129 tracer signal in the Eurasian (especially the Amundsen) Basin , and lower I129 concentrations in was characterized by higher
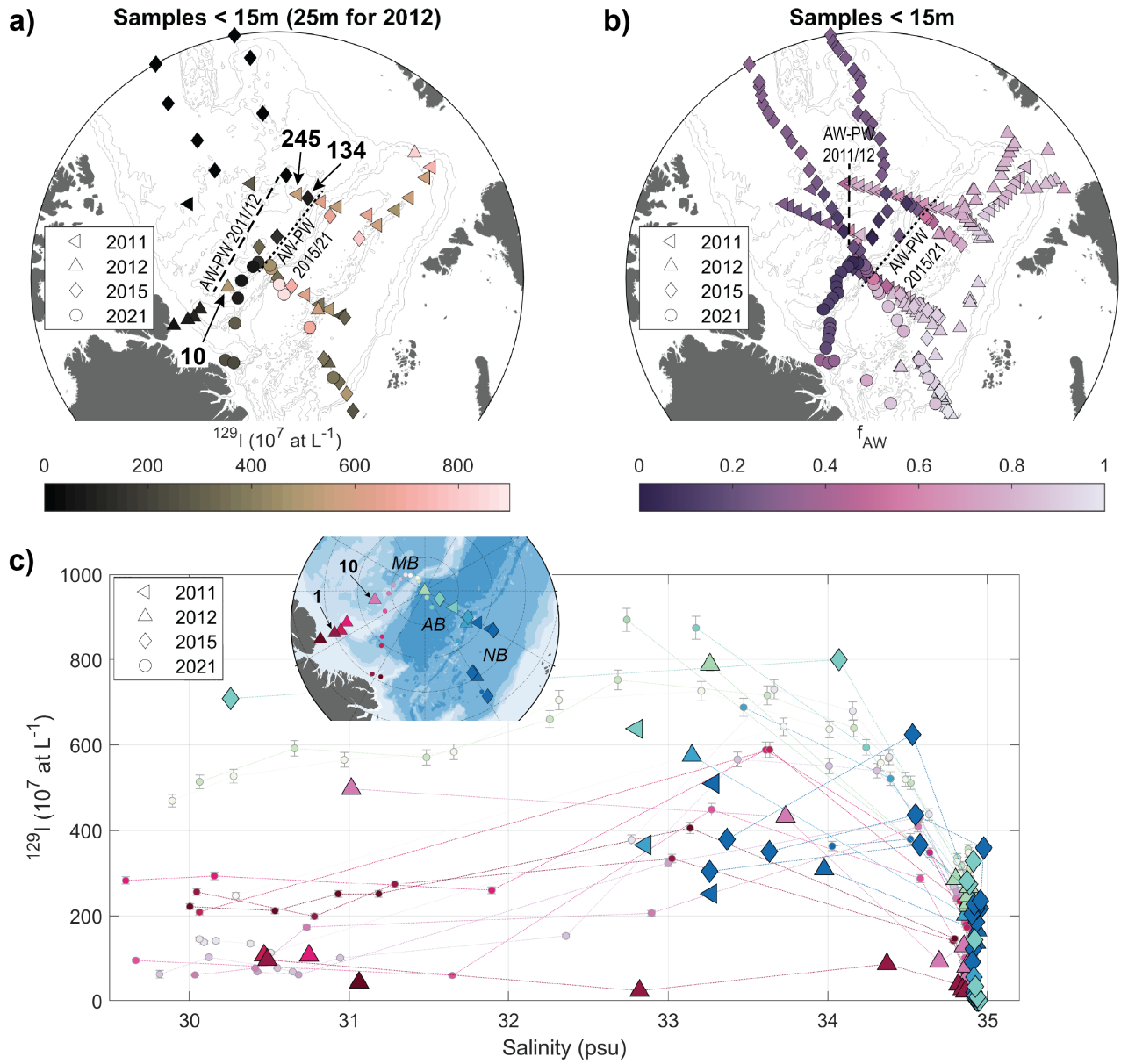
28

Figure 10. (a) Isosurface map of ~~I129~~ ^{129}I concentrations in the surface (< 15 m depth for 2011, 2015, 2021; 25 m depth for 2012 due to sampling depth resolution). The front between Atlantic- and Pacific-derived surface waters based on ~~I129~~ ^{129}I concentration for 2011/12 is indicated by a dashed line, and for 2015/21 by a dotted line. (b) Isosurface map of Atlantic Water fractions (f_{AM}) derived from salinity and N:P ~~fractions~~ratios, for all available data from the surface layer from the same expeditions as in (a). The front between Atlantic- and Pacific-derived surface waters based on N:P ratios for 2011/12 is indicated by a dashed line, and for 2015/21 by a dotted line. (c) Plot of ~~I129~~ ^{129}I concentration against ~~absolute~~ practical salinity for available stations from 2011, 2012, 2015, 2021. ~~Note that~~ The 2021 data is the same as in Fig. 5c. Stations are color-coded by region, following the color-coding for SAS2021 stations.

concentrations in the Amundsen Basin compared to the Makarov Basin and north of Greenland (Fig. 10a) in all years. While the surface Makarov Basin (close to the North Pole) appeared to be dominated by Pacific Water in 2021, one station (station 10) suggested a stronger Atlantic Water signal in this region in 2012. A similar trend was observed further upstream. Station 245

680 indicated a stronger Atlantic Water signal in 2011, while station 134 showed a lower tracer concentration and hence less Atlantic Water at a similar location in 2015 (see also Wefing et al. (2021) for further discussion).

Atlantic and Pacific Water fractions for the same datasets were also calculated based on the N:P method, again following the method by Bauch et al. (2011, see also Section 4.2), albeit using a three-end-member model of Atlantic, Pacific, and freshwater

685 due to limited availability of δ^{18}O data (~~calculations outlined in~~ Appendix B). Atlantic Water fractions in the surface were limited to the Eurasian side of the Lomonosov Ridge in 2015 and 2021 (Fig. 10b). In 2011, however, high Atlantic Water fractions were observed in the Makarov Basin, extending to the Alpha-Mendeleyev Ridge, which is in line with the ~~I129~~ ^{129}I distribution.

~~It should be noted that the~~ The sampling resolution for ~~I129~~ ^{129}I was sparse, especially in the earlier years and often limited

690 to "surface samples", with depths varying between 5 and 30 m. The high-resolution ~~I129~~ ^{129}I sampling in the upper 50 m at several SAS2021 stations showed significant variation in the ~~I129~~ ^{129}I concentration in this highly dynamic layer (Fig. 3a, c and 5c). To take varying sampling depths and changes in the water mass composition into account, all samples collected in the vicinity of the SAS2021 stations in different years were added to the SAS2021 ~~I129-Salinity~~ ^{129}I-Salinity plot (Fig. 10c). The available depth profile from the Lincoln Sea ~~from~~ in 2012 (station 1), upstream of the SAS2021 stations north of Greenland,

695 clearly reflected Canada Basin waters carrying very low ~~I129~~ ^{129}I concentrations across the entire Polar Surface Water layer (and below). In contrast, the higher ~~I129~~ ^{129}I concentrations observed in the SAS2021 stations located further downstream, north of Greenland (dark red circles), pointed to a significantly higher fraction of Atlantic-origin water being transported to this region in 2021, presumably from the Amundsen Basin. As also seen in the isosurface map (Fig. 10a), station 10 from 2012 showed higher ~~I129~~ ^{129}I concentrations compared to 2021 samples from nearby stations and corresponding salinities.

700 ~~I129 concentrations observed~~ ^{129}I concentrations measured at this location in the Makarov Basin in 2012 ~~almost matched~~ were comparable to those observed on top of the Lomonosov Ridge, close to the North Pole, in 2021 (light green circles).

In summary, ~~both~~ the distribution of ~~I129 and~~ ^{129}I and the N:P-based Atlantic Water fractions ~~, suggested~~ suggested ~~that~~ Atlantic-origin water ~~reaching further~~ extended farther across the Lomonosov Ridge ~~and~~ into the Makarov Basin in

705 2011 and 2012, compared to the years 2015 and ~~2021, implying a change~~ 2021. This implies a shift in the surface water circulation ~~. Temporal changes in the Atlantic-Pacific Water front have been investigated in earlier studies, using both, nutrient relationships (e.g., Alkire et al., 2007, 2015) and I129 (Karcher et al., 2012; Smith et al., 2021). They have generally been found to be associated with different states of atmospheric circulation patterns and coupled oceanic responses, described by indices such as the Arctic Oscillation (AO; e.g., Morison et al., 2012), the Arctic Ocean Oscillation (AOO; e.g., Proshutinsky et al., 2015~~

710 ~~, or the Arctic Dipole (AD; e.g., Polyakov et al., 2023).~~

pattern. Smith et al. (2021) found that changes in the surface ~~I129~~ ^{129}I distribution across the Arctic Ocean ~~reflect~~ reflected a change from a cyclonic circulation mode associated with a positive AO index in the mid-1990s to an anti-cyclonic circulation mode along with a negative AO index in the 2000s ~~.~~ (Fig. A7). This change was accompanied by a shift in the Atlantic-Pacific Water front from the Alpha-Mendeleyev Ridge (1990s) to the Lomonosov Ridge (2015). Our analysis of ~~I129~~ ^{129}I concentrations between 2011 and 2021 indicated that ~~this shift was still ongoing~~ the position of the front still changed between 2011 and 2015, but ~~the position of the front did not change further~~ remained stable between 2015 and 2021. Polyakov et al. (2023) described an increasingly positive phase of the Arctic Dipole (AD+) between 2007 and 2021, leading not only to enhanced inflows of Atlantic Water through the Barents Sea Opening compared to Fram Strait, but also to a shift in the alignment of the Transpolar Drift from the Amerasian Basin towards the Lomonosov Ridge. This is ~~again~~ further supported by the change in surface ~~I129~~ ^{129}I distribution, where the available tracer data suggests that a strong shift occurred between 2011 and 2015.

4.3.1 ~~Changes in the Atlantic Layer and below~~

~~PDFs G(t) for matching stations from different sampling years (2011 - 2021). Rows are different depths (300, 500, 1000), columns are different regions/basins. Stations and regions are shown in the map. GR: Gakkel Ridge, AB: Amundsen Basin, MB: Makarov Basin, CB: Canada Basin. TTD parameters can be found in Appendix C.~~

~~For the Atlantic Layer, we focused on temporal changes in circulation times and transport characteristics. PDFs were obtained from the TTD model with I129 and U236 for available stations within different Arctic regions, spanning the years 2011 to 2021~~

4.4 Provenance of Halocline Waters

Below the surface layer, which was found to be clearly influenced by Pacific Water, halocline waters reside. Based on their T and S properties, halocline layer samples from the Amundsen Basin (station 8 and 16) were associated with the LHC, which in the Eurasian Basin is formed through repeated winter convection cycles north of the Barents Sea, as well as by advection of low-salinity shelf water, primarily from the Laptev Sea (Rudels et al., 1996). The halocline samples from the Makarov Basin (station 28) and north of Greenland (station 46) had practical salinities slightly below 34. They were, therefore, classified as UHC waters by hydrographic properties and are thought to be derived from Pacific inflow but also influenced by the East Siberian Sea (e.g., Anderson et al., 1994, 2017). However, this is not supported by the radionuclide concentrations. The similar location of the 100 m samples from the different stations in the dual-tracer plot (Fig. ~~9, see Table 1 for details on available tracer data). PDFs from different years were compared at different depth layers where most samples were available (300, 500, 1000).Note different scales for G(t).~~ 6) suggested a common origin or formation region and transport route for these halocline waters, before they are transported across the Arctic Ocean towards Greenland. This was also supported by the additional available ^{129}I data, where samples from the Amundsen and Makarov Basins showed similar ^{129}I concentrations throughout the LHC layer (Fig. 5c and Fig. A6a). Furthermore, the comparably high tracer concentrations, substantially higher than closer to the surface, suggested only little Pacific-origin water but a significant fraction of tracer-labeled NCC-origin waters, which

were transported along the Eurasian shelf and contributed to the formation of halocline waters along their way. Based on ^{129}I and ^{236}U, we conclude that halocline waters formed from Atlantic-origin waters were present throughout the entire study area, including the Makarov Basin and the area north of Greenland.

~~For the Eurasian Basin (stations at Gakkel Ridge and Amundsen Basin), the PDFs showed an increase of mean and mode ages over time, especially from 2015 to 2021. Δ~~ The distribution of the NO parameter (NO = $(9 \times NO_3^-) + O_2$, Broecker (1974)) supports this finding. Alkire et al. (2019) used an NO concentration of 400 mmol m^{-3} to discriminate Atlantic from Pacific waters, with lower concentrations indicative of Atlantic Water. The distribution of NO derived from the SAS2021 dataset at a practical salinity of 34 did not show ~~a clear trend and was largely similar in all years~~ large variability across the study area (Fig. ~~??). These findings suggest a slowdown in the~~ A6b). NO concentrations in the Amundsen and Makarov Basins and north of Greenland were all below 400 mmol m^{-3}, hence pointing to Atlantic origin.

4.5 Circulation of Waters in the Atlantic Layer

The mode ages obtained from the TTD model for AAW allow to assess the circulation of Atlantic Water ~~to the Amundsen Basin between 2015 and 2021 that was not accompanied by an increase in mixing along the flow path~~ in the central Arctic at mid-depths. Here we exclude the Nansen Basin from further interpretation since this station is not located downstream of the initialization point of the Atlantic Layer input function (the St. Anna Trough, where FSBW and BSBW merge), and the TTD analysis is not expected to provide meaningful results. This was already shown in earlier studies (Wefing et al., 2021; Raimondi et al., 2024; .

~~PDFs from the Makarov Basin showed a similar behavior between 2015 and 2021 down to 500 depth. As for the Amundsen Basin , Δ remained largely unchanged over time. In contrast to the Amundsen Basin, mode ages in~~ The decrease in mode ages from the central Eurasian Basin towards the Lomonosov Ridge suggests that waters in the mid-depth Atlantic layer are transported faster close to the ridge, which could be explained by transport in a branch of the Arctic Ocean Boundary Current flowing along the Amundsen Basin side of the Lomonosov Ridge. The same spatial pattern was observed by Körtke et al. (2024), investigating tracer ages from CFC-12 and SF$_6$, as well as Pasqualini et al. (2024), from ^{3}H-^{3}He ages. However, interestingly, Δ/Γ ratios did not suggest very advective transport at station 20, but rather increased from the interior Eurasian Basin towards the Lomonosov Ridge, indicating more mixing along the flow. In the Makarov Basin, north of Greenland, and in the Canada Basin, low Δ/Γ ratios and high mode ages pointed to more advective flow, and longer current pathways, confirming earlier studies on TTDs in the Canada Basin (Smith et al., 2011; Wefing et al., 2021; Raimondi et al., 2024). The significantly higher mode ages in the Makarov Basin ~~in 2015 and 2021 did not show a clear increasing trend.~~ suggest that waters have been transported along a different (longer) loop compared to the Amundsen Basin. A difference in water mass ages between both sides of the Lomonosov Ridge was also observed by Tanhua et al. (2009) and Gerke et al. (2024), albeit in mean ages derived from gas tracers. Both studies found higher mean ages, i.e., a slower ventilation, in the Makarov Basin compared to the

Amundsen Basin, with a sharp front over the Lomonosov Ridge. This is in line with our findings based on ^{129}I and ^{236}U, confirming the study by Raimondi et al. (2024) that anthropogenic radionuclides and gas tracers such as CFCs and SF$_6$ act as
780   similar Atlantic Water tracers in the Arctic Ocean once the Atlantic Water layer is isolated from atmospheric gas exchange.

~~In the Canada Basin samples from different years were only available at 500 depth. While no change in the mode ages was observed,~~ The binary mixing model and the large width of the unimodal TTD indicated that AAW north of Greenland represents a mixture of Atlantic Water that has circulated in the boundary current through the "long loop" (Canada Basin) and
785   the ~~shape of the PDF was altered due to a decrease in both Γ and Δ from 2015 to 2020~~ "short loop" (Eurasian Basin) and hence a wide distribution of circulation times. The mean ages derived from the bimodal TTD, accounting for two main pathways and associated circulation times, were more reasonable than those from the unimodal TTD, which on average even exceeded those from the Canada Basin (Fig. ~~??).~~
~~Overall, the comparison of TTD parameters from 2015 and 2021 showed little to no changes in mixing within the~~ 7a). Also
790   the more rapid decrease of the bimodal TTD at old ages (Fig. 8d), similar to the Canada and Amundsen Basin, points to the use of the bimodal TTD to describe Atlantic Water transport ~~(TTD parameter Δ) in different locations in the Amundsen Basin, the Makarov Basin close to the Lomonosov Ridge, and a location in the Canada Basin. Mode ages have been shown to be~~ north of Greenland which considers the two branches of Atlantic Water being advected from the Amundsen and Canada Basins. This applies to other regions of the Arctic Ocean as well, such as the mixing of Atlantic and Pacific-derived water over the Chukchi
795   Sea shelf described in Smith et al. (2022).

4.6   Temporal Changes in Atlantic Water Circulation

Mode ages are a good measure of lateral circulation times of Atlantic Water (Smith et al., 2011; Wefing et al., 2021; Raimondi et al., 2024) and the observed increase in mode ages in the Amundsen and Canada Basins between 2015 and 2021 suggests a
800   slowdown in Atlantic Water circulation~~between 2015 and 2021.~~

4.6.1   ~~Comparison to temporal variability observed with gas tracers~~

~~Changes in~~ . Over the same period, little to no changes in mixing within the Atlantic Water transport ~~and ventilation up to 2021 have also been investigated using gas tracers (Gerke et al., 2024). Their study was~~ were observed (TTD parameter Δ) in different locations in the Amundsen Basin, the Makarov Basin close to the Lomonosov Ridge, and a location in the Canada
805   Basin. Our findings confirm the results by Gerke et al. (2024), who observed a similar trend based on CFC-12 and SF$_6$ data from SAS21 ~~as well as from~~ and earlier years (1991, 2005, 2015)~~using the "classical" TTD method (see Raimondi et al. (2024) for differences to our method) and focusing on the obtained mean ages. Overall, Gerke et al. (2024) observed a similar trend to this study, with an increase in~~ . They found increasing mean ages from 2015 to 2021 ~~across~~ throughout the entire Atlantic Water layer in the Amundsen Basin. ~~Since the gas tracers are introduced from exchange with the atmosphere, the increase in mean~~
810   ~~ages was interpreted as a slowdown in ventilation in 2021 compared to 2015 (and 2005). In the Arctic Ocean, the mid-depth~~

33

~~Atlantic Layer is isolated from the atmosphere after subduction in the region of the St. Anna Trough, hence the increase in mean ages obtained from gas tracers can also be interpreted as a measure for Atlantic Water circulation times, similar to the radionuclide tracers (Gerke et al., 2024; Raimondi et al., 2024). Gerke et al. (2024) speculate about a decrease in the strength~~, which they attributed to a weakening of the Arctic Ocean Boundary Current, leading to a slowdown in the lateral circulation of Atlantic Water.

~~Körtke et al. (2024) investigated temporal changes in Atlantic Water pathways based on tracer ages obtained from CFC-12 and SF$_6$. They largely confirmed the different circulation patterns under changing conditions of the Arctic Oscillation (AO) index suggested by Karcher et al. (2012) and Smith et al. (2021). Lower Atlantic Water tracer ages in the~~ A decrease in the strength of the boundary current has been observed in tracer studies between the mid-1990s ~~were attributed to a strong boundary current connected to a positive AO index. Increased tracer ages in 2005~~ and 2015~~were interpreted as a weakening of the boundary current and coincided with phases of largely negative or mixed AO index (Fig. ??). In addition, tracer age changes are also attributed to changes in the Atlantic Water pathways (see e.g. Fig. 7 in Körtke et al., 2024)~~, which was related to a decrease in the AO index (Smith et al., 2021; Körtke et al., 2024). Both studies found an increase in Atlantic Water circulation times over that period. Since 2015, the AO index has largely been positive, based on which a decrease in Atlantic Water ~~tracer ages/circulation times~~ circulation times between 2015 and 2021 could be expected. This is not observed in our study region. However, it is unclear how fast circulation in the mid-depth Atlantic Layer responds to changes in atmospheric conditions and surface layer circulation.

Another reason for changes in mean ages~~observed both with~~, as indicated by gas tracers and radionuclides, could be circulation changes in the formation region of ~~mid-depths~~ mid-depth waters, i.e., Fram Strait and the Barents Sea. Polyakov et al. (2023) describe fluctuations in the inflow of Atlantic Water through the Barents Sea Opening compared to Fram Strait. This would likely affect radionuclide tracer concentrations introduced into the mid-depth Atlantic layer through different mixing between the different branches carrying different tracer concentrations ~~(Casacuberta et al., 2018; ?)~~ (Casacuberta et al., 2018; Pérez-Tribouill... and gas tracer input functions depending on surface saturation levels (e.g., Raimondi et al., 2021).

The mechanism driving the observed increase in Atlantic Water circulation times from 2015 to 2021 remains unclear and further research is needed in this regard. This could include the simulation of Atlantic Water tracers in circulation models as done in Karcher et al. (2012); Smith et al. (2021). Also, ~~a longer period of data coverage is probably needed~~ an extended temporal coverage with high spatial sampling resolution across multiple Arctic basins is probably required for the mid-depth layer, since changes ~~happen slower than~~ occur more slowly than in the surface layer. To better understand the link to atmospheric conditions, ~~data~~ observations spanning phases of different atmospheric conditions ~~is~~ are required, such as the change in AO index from the 1990s to the 2000s.

5 Conclusion and Outlook

In this study, we ~~used~~ utilized the combination of the radionuclides ~~I129 and U236~~ ^{129}I and ^{236}U to assess Atlantic Water pathways, mixing, and circulation times, as well as the Pacific Water lateral extent in the central Arctic Ocean in 2021 and to study changes in Atlantic Water circulation between 2011 and 2021.

Along the transect of the SAS2021 expedition, covering the Nansen, Amundsen, and Makarov Basins, as well as the region of the Lincoln Sea north of Greenland, we observed a sharp drop in radionuclide concentrations in the surface layer between the Amundsen and the Makarov ~~Basin~~Basins, directly at the Lomonosov Ridge. ~~This was attributed~~ We attributed this to a significant fraction of Pacific Water on the Makarov Basin side, carrying low radionuclide concentrations, ~~and~~ which was qualitatively supported by Pacific water fractions calculated ~~from~~ with the N:P (nitrate to phosphate) ~~ratios.~~ method. Regarding the temporal evolution of the lateral extent of Pacific Water, we found that the Atlantic-Pacific Water front was located further in the Makarov Basin in 2011 and 2012 compared to 2015 and 2021, when it was aligned with the Lomonosov Ridge. The same pattern was observed based on the N:P method. This supports earlier findings by Smith et al. (2021), who describe the shift of the Atlantic-Pacific Water front from the Alpha-Mendeleyev Ridge in the 1990s to the Lomonosov Ridge in 2015 due to changes in the Arctic Oscillation index. Our data indicates that the shift towards the Lomonosov Ridge continued through 2011 and 2012. By 2015, the front had aligned with the Lomonosov Ridge, and was located at a similar location in 2021.

For the halocline layer, we found similar radionuclide concentrations across the entire transect, ~~pointing to~~ indicating a common formation area and transport route of the halocline waters. ~~Comparably high~~ High tracer concentrations furthermore indicated the presence of Atlantic-origin waters in the halocline, suggesting that these waters ~~are~~ were formed around the Barents Sea, where they picked up the tracer signal of the surface layer input function.

This dataset includes the first available ~~I129 and U236~~ ^{129}I and ^{236}U data from the area north of Greenland~~and in~~. In both, the surface layer (except the halocline) ~~as well as~~ and the mid-depth Atlantic layer, tracer concentrations indicated that these waters were a mixture of Canada Basin and Amundsen Basin waters. In the mid-depth Atlantic layer, the TTD model provided mean ages, mode ages, and mixing properties for the flow of Atlantic Water through the Arctic Ocean. Confirming earlier studies based on gas tracers (CFCs and SF$_6$), we found an increase in mean (and mode) ages when crossing the Lomonosov Ridge from the Amundsen into the Makarov Basin, implying a longer transport route.

~~To assess temporal changeover the past decade, we collated all available I129 and U236 data from the Arctic Ocean from earlier studies. In the surface layer, we found a change in the Atlantic-Pacific Water front, which was aligned with the Lomonosov Ridge in 2015 and 2021, but located further in the Makarov Basin in 2011 and 2012. The same pattern was found based on N:P ratios from the same years. One explanation for this change in the Pacific Water extent lies in circulation changes associated with atmospheric circulation patterns, described by indices such as the Arctic Oscillation index or the Arctic Dipole. Smith et al. (2021) describe the shift of the Atlantic-Pacific Water front from the Alpha-Mendeleyev Ridge in the 1990s to the~~

Lomonosov Ridge in 2015 due to changes in the Arctic Oscillation index. Also, the increasingly positive phase of the Arctic Dipole between 2007 and 2021 was associated with a shift in the alignment of the Transpolar Drift from the Amerasian Basin
880 towards the Lomonosov Ridge (Polyakov et al., 2023). Our data supports these findings and indicates that the shift towards the Lomonosov Ridge continued through 2011 and 2012. By 2015, the front had aligned with the Lomonosov Ridge, and was located at a similar location in 2021.

In the mid-depth Atlantic layer, we found Regarding temporal changes, we observed an increase in mean and mode ages obtained from the TTD model in the Amundsen Basin from 2015 to 2021. The same trend was observed by Gerke et al. (2024)
885 using the TTD model with CFC-12 and SF$_6$. This implies either a slowdown in Atlantic Water circulation, which could be attributed to a decrease in the strength of the Arctic Ocean Boundary Current (Gerke et al., 2024)(as also suggested by Gerke et al., 2024), different Atlantic Water pathways (as discussed in Smith et al., 2021; Körtke et al., 2024), or changes in the inflow region of the tracers (such as changes in Fram Strait and Barents Sea Water inflow as a consequence of the Arctic Dipole state, Polyakov et al., 2023). Further research is needed to identify the mechanism behind these changes.

890

The atlantification of the Arctic Ocean is not no longer restricted to the Eurasian Basin anymore, but was recently found to have reached , as recent findings indicate that it has extended into the Makarov Basin (Polyakov et al., 2025), once more again confirming that the Arctic Ocean is undergoing drastic changes. How these changes will affect the Arctic system, from the uptake of anthropogenic Carbon to consequences for ecological systems, remains to be investigated. As part of this, under-
895 standing and monitoring changes in the Atlantic Water circulation is crucial. Our study not only confirms that the anthropogenic radionuclides I129 and U236 are powerful Atlantic Watertracers but also that the available tracer data set collected during ^{129}I and ^{236}U are effective tracers of Atlantic Water, and highlights the value of the tracer dataset collected over the past decade is of great value and can now be used to assess for assessing temporal changes. During the SAS2021 expedition, an effort was made to couple the sampling of different circulation and ventilation tracers. Following the recent study by Raimondi et al.
900 (2024), these different kinds of this set of various tracers can be combined in future studies, allowing, for instance, a more comprehensive assessment of anthropogenic Carbon stored in the Arctic Ocean. To this aim, long-term ventilation tracers such as Carbon-14 and Argon-39 should be included and will allow extending such studies to deeper and older water masses.
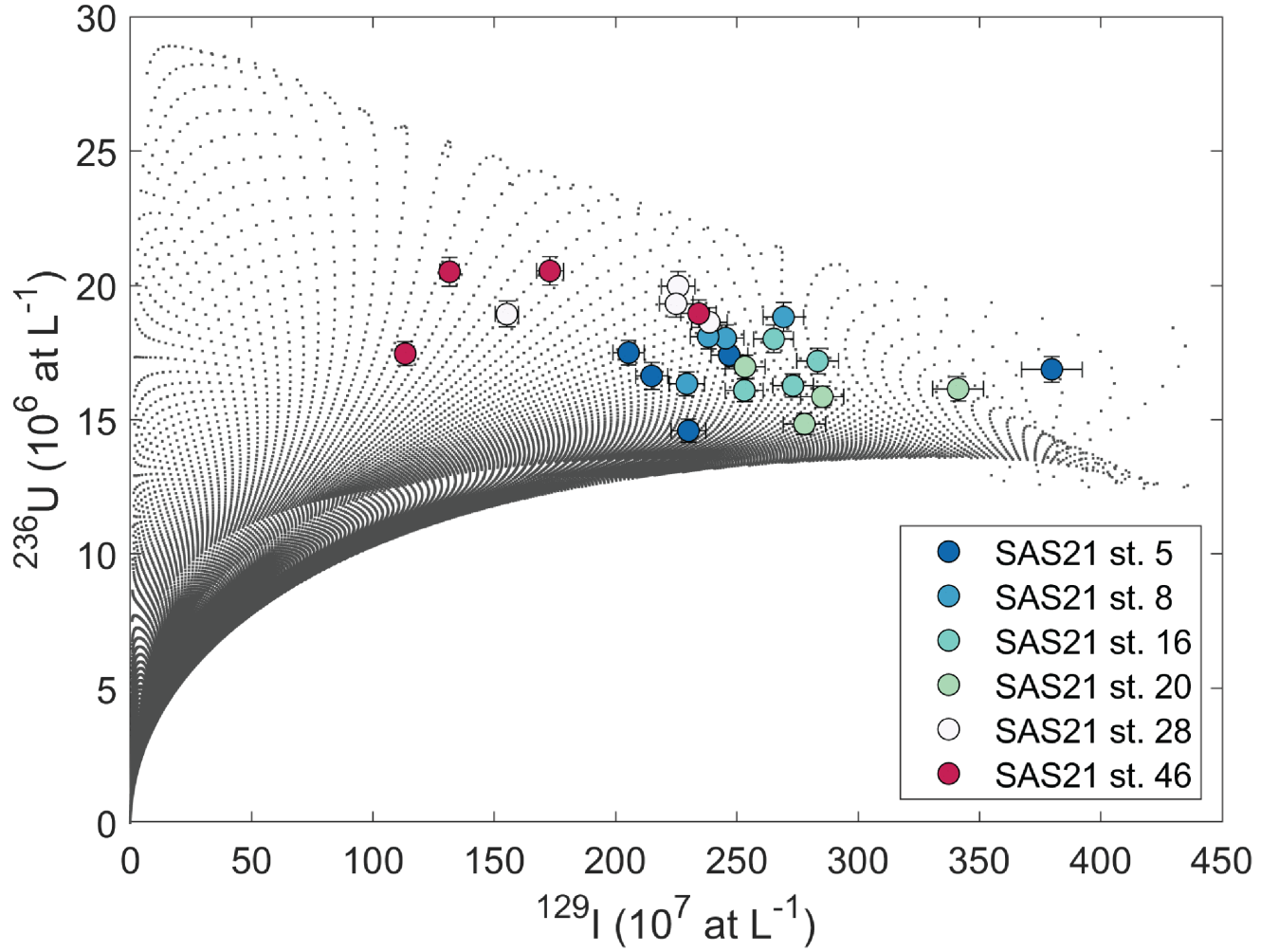
Figure A1. $\Delta - \Gamma$ grid in ^{236}U-^{129}I space for the determination of TTD parameters according to "Smith's method" (see Raimondi et al. (2024) for detailed explanation). SAS2021 samples are plotted on top, color-coded by station.
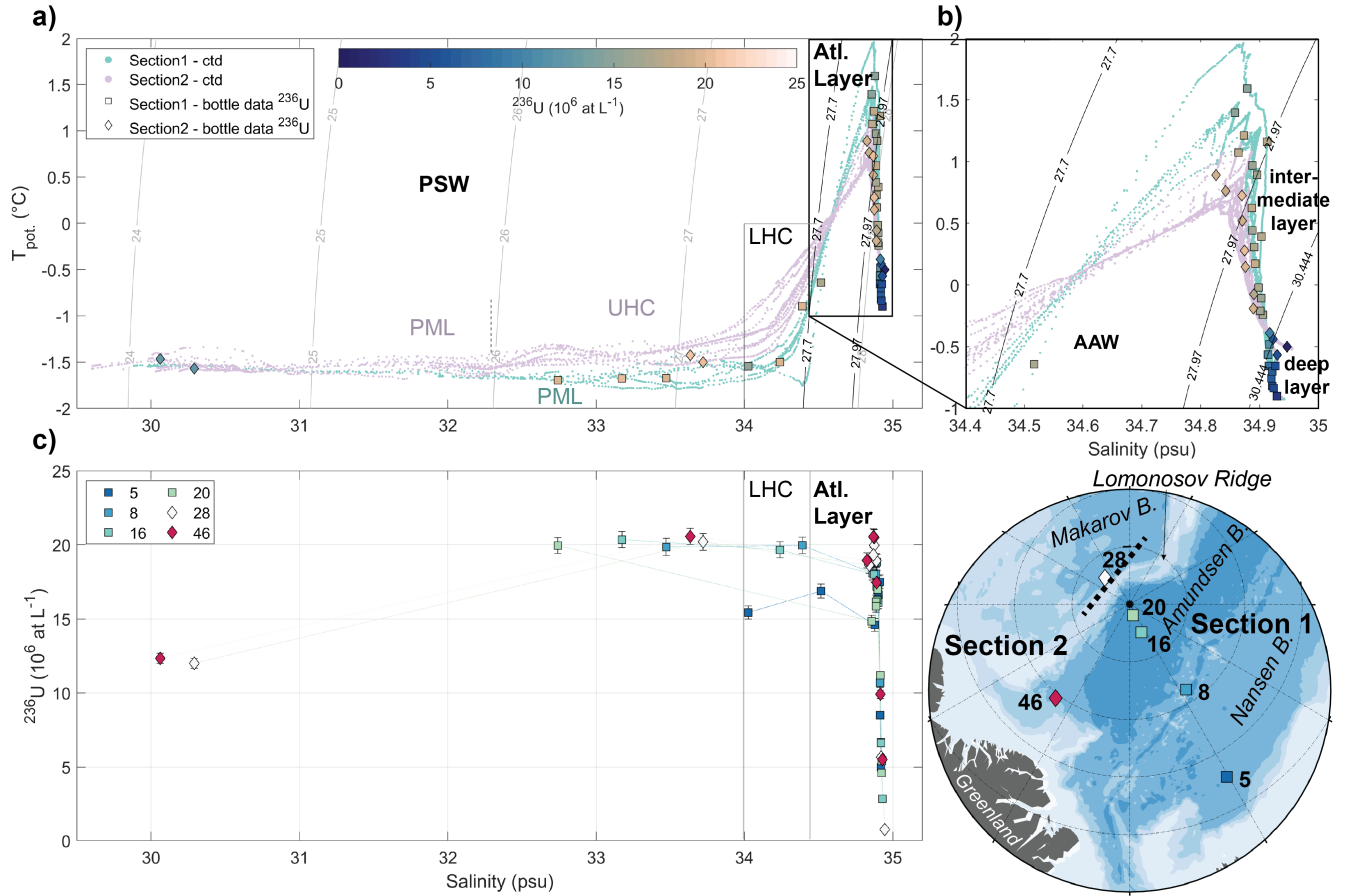
Figure A2. (a) T-S plot (~~conservative~~ potential temperature against ~~absolute~~ practical salinity) with ~~U236~~ ^{236}U concentrations color-coded and different water masses indicated (PSW: Polar Surface Water, PML: Polar Mixed Layer, UHC: upper halocline, LHC: lower halocline, AAW: Arctic Atlantic Water). Teal and purple dots are 1 m-binned ~~etd~~ CTD data from Section 1 and 2, respectively. Square and diamond data points are bottle file data from Section 1 and 2, respectively. (b) close-up of the Atlantic Layer (black box in a). (c) Plot of ~~U236~~ ^{236}U concentration against ~~absolute~~ practical salinity with stations color-coded.
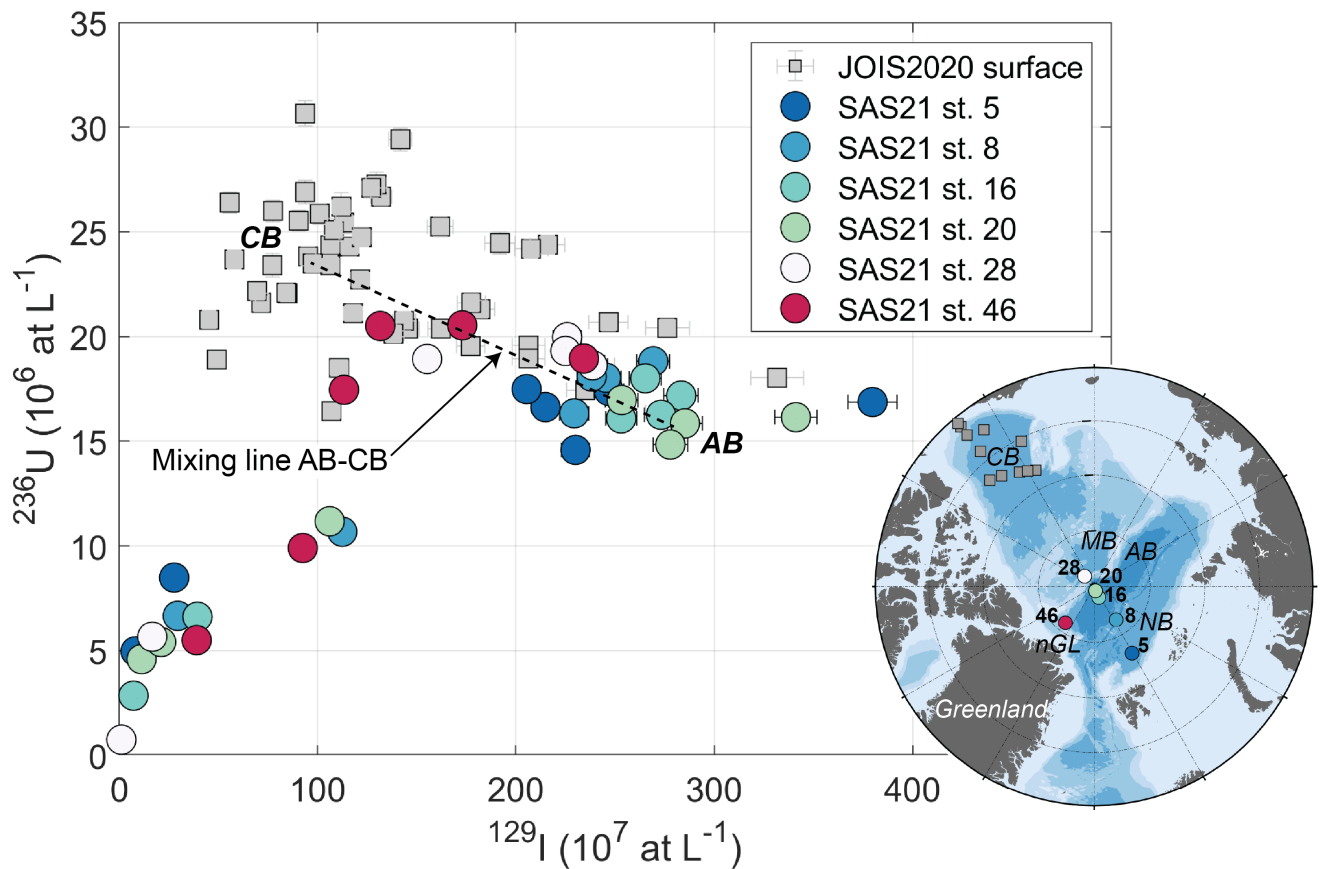
Plot of ~~U236 against I129~~ ^{129}I concentrations for samples from the Atlantic Layer. SAS2021 PSW samples are color-coded by station. CB: Canada Basin, AB: Amundsen Basin. Samples from the Atlantic Layer in the Canada Basin collected in 2020 (JOIS2020, Payne et al., 2024) are shown in grey squares.

Plot of ~~U236 against I129~~ ^{129}I concentrations for samples from the Atlantic Layer. SAS2021 PSW samples are color-coded by station. CB: Canada Basin, AB: Amundsen Basin. Samples from the Atlantic Layer in the Canada Basin collected in 2020 (JOIS2020, Payne et al., 2024) are shown in grey squares.

Figure A3. Plot of ~~I129 concentration~~ ^{236}U against ~~absolute salinity with data color-coded by (a) meteoric water fraction f_MW, (b) sea-ice meltwater fraction f_SIM, (c) Pacific Water fraction f_PAC. (d) Plot of I129 concentration corrected by meteoric water fraction f_MW against absolute salinity with stations color-coded.~~ ~~Plot of U236 against I129~~ ^{129}I concentrations for samples from the Atlantic Layer. SAS2021 PSW samples are color-coded by station. CB: Canada Basin, AB: Amundsen Basin. Samples from the Atlantic Layer in the Canada Basin collected in 2020 (JOIS2020, Payne et al., 2024) are shown in grey squares.

Isosurface maps of (a) I129 concentration and (b) the NO parameter (Broecker, 1974; Alkire et al., 2019) at practical salinity $S_P = 34 \pm 0.5$. TTD parameters Γ, Δ, and t_{mode} plotted against sampling year. Rows are different depths (300, 500, 1000 m), columns are different regions/basins. Stations and regions are shown in the map in Fig. 9. Data can be found in Appendix C.

Isosurface maps of (a) I129 concentration and (b) the NO parameter (Broecker, 1974; Alkire et al., 2019) at practical salinity $S_P = 34 \pm 0.5$.

TTD parameters Γ, Δ, and t_{mode} plotted against sampling year. Rows are different depths (300, 500, 1000 m), columns are different regions/basins. Stations and regions are shown in the map in Fig. 9. Data can be found in Appendix C.

Figure A4. $\Delta - \Gamma$ grid in U236-I129 space for the determination of TTD parameters according to "Smith's method" (see Raimondi et al. (2024) for detailed explanation). SAS2021 samples are plotted on top, color-coded by station.
Isosurface maps of (a) I129 concentration and (b) the NO parameter (Broecker, 1974; Alkire et al., 2019) at practical salinity $S_P = 34 \pm 0.5$.
TTD parameters Γ, Δ, and t_{mode} plotted against sampling year. Rows are different depths (300, 500, 1000 m), columns are different regions/basins. Stations and regions are shown in the map in Fig. 9. Data can be found in Appendix C.
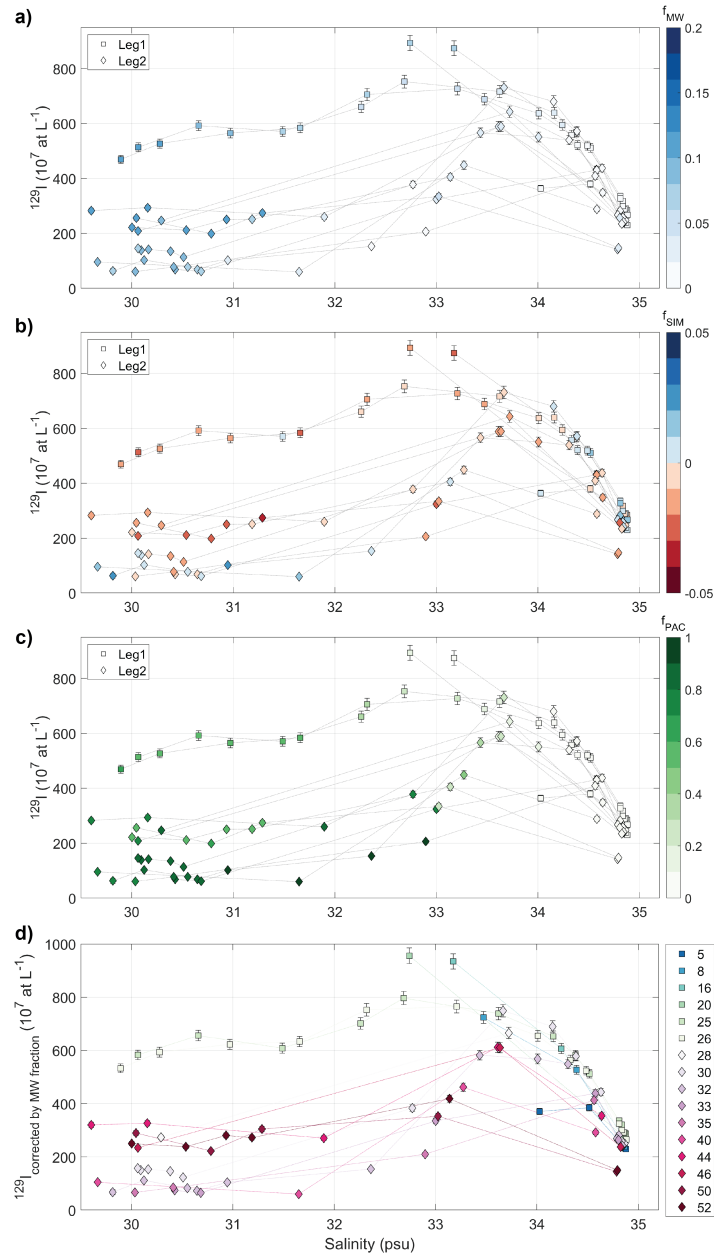
Figure A5. Plot of [129]I concentration against practical salinity with data color-coded by (a) meteoric water fraction f_{MW}, (b) sea-ice meltwater fraction f_{SIM}, (c) Pacific Water fraction f_{PAC}. (d) Plot of [129]I concentration corrected by meteoric water fraction f_{MW} against practical salinity with stations color-coded.
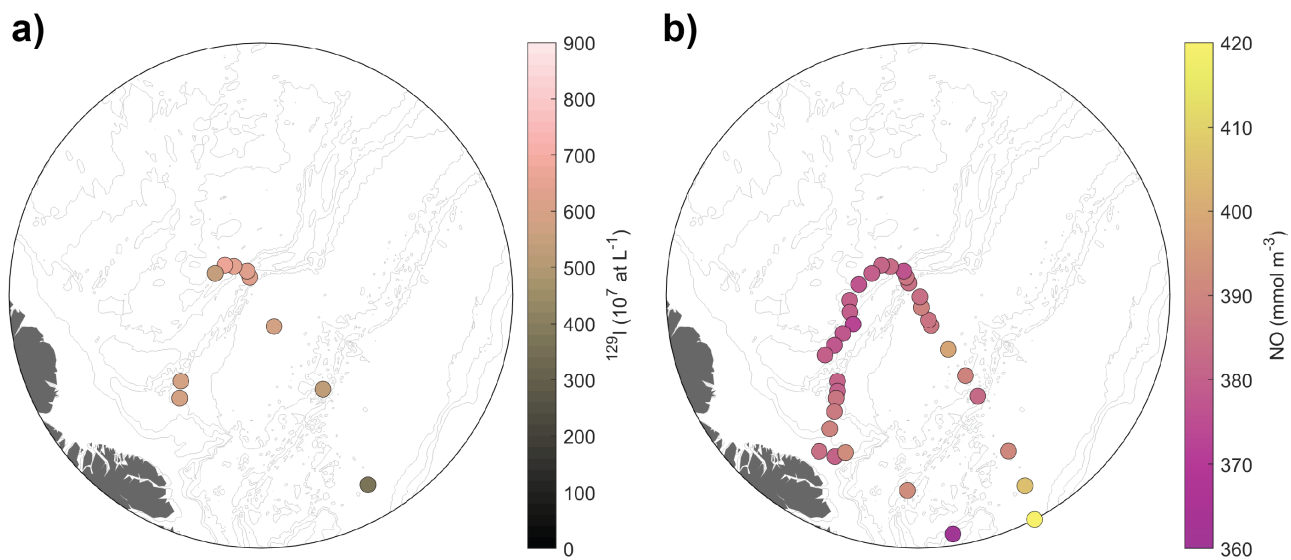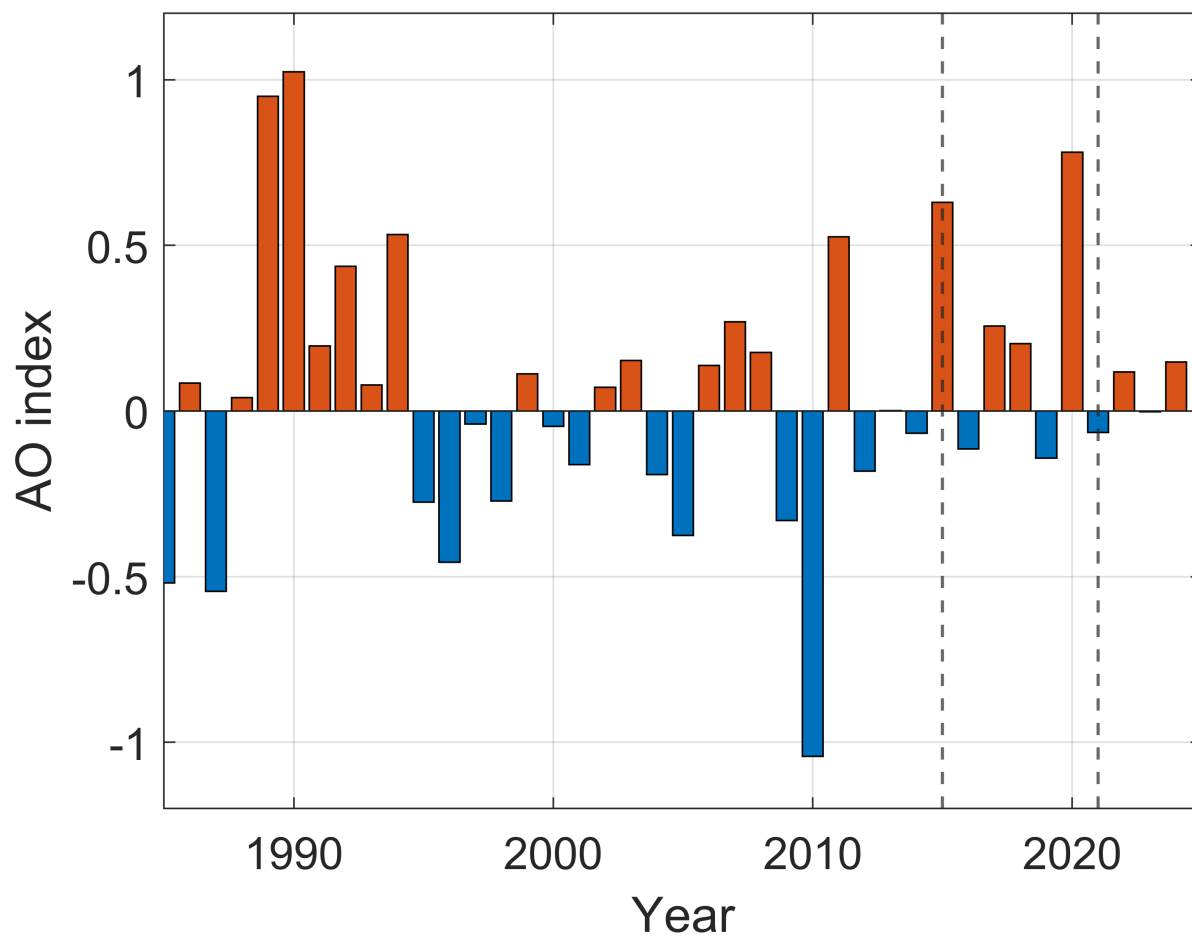
Figure A6. Isosurface maps of (a) [129]I concentration and (b) the NO parameter (Broecker, 1974; Alkire et al., 2019) at practical salinity $S_P = 34 \pm 0.5$.

Figure A7. Arctic Oscillation (AO) index (yearly average). Tracer sampling years 2015 and 2021 are indicated as dashed lines. Figure modified after Fig. 6d in Körtke et al. (2024). Arctic Oscillation Data downloaded from: https://www.cpc.ncep.noaa.gov/products/precip/ CWlink/daily_ao_index/ao.shtml (28.02.2025).

Appendix B: Calculation of Atlantic and Pacific Water ~~fractions~~ Fractions with ~~three-end-member model~~Three-End-Member Model

910 Atlantic and Pacific Water fractions were calculated based on the N:P method, following the method by Bauch et al. (2011), but using a three-end-member model of Atlantic Water (AW), Pacific Water (PW), and freshwater (FW) due to limited availability of δ^{18}O data. Endmember values were taken from Bauch et al. (2011), for the freshwater endmember we used the river water endmember therein. The three-component mass balance is the following:

$$f_{AW} + f_{PW} + f_{FW} = 1 \tag{B1}$$

915 $$f_{AW} S_{AW} + f_{PW} S_{PW} + f_{FW} S_{FW} = S_{meas} \tag{B2}$$

$$f_{AW} P_{AW} + f_{PW} P_{PW} + f_{FW} P_{FW} = P_{meas} \tag{B3}$$

with $S_{AW} = 34.92$, $S_{PW} = 32.7$, $S_{FW} = 0$, $P_{AW} = 0.0596 \cdot N_{meas} + 0.1139$, $P_{PW} = 0.0653 \cdot N_{meas} + 0.9400$, $P_{FW} = 0.1$.

Hydrographic and nutrient data for expeditions PS78 (2011), PS80 (2012), and PS94 (2015) can be found on PANGAEA:
920 https://doi.org/10.1594/PANGAEA.832164, https://doi.org/10.1594/PANGAEA.774181, https://doi.org/10.1594/PANGAEA.834081, https://doi.org/10.1594/PANGAEA.819452, https://doi.org/10.1594/PANGAEA.868396, https://doi.org/10.1594/PANGAEA.859559. Hydrographic and nutrient data for expedition HLY1502 (2015) was taken from the GEOTRACES Intermediate Data Product: https://doi.org/10.5285/cf2d9ba9-d51d-3b7c-e053-8486abc0f5fd.

Appendix C: TTD ~~temporal results~~Temporal Results

925 Tables with TTD parameters Γ, Δ, and t_{mode} for the different regions/basins, depths (300, 500, 1000 m), and sampling years shown in Fig. ??A.

Table C1. Gakkel Ridge

Depth (m)	TTD parameter (years)	Year 2011 Station 204 val	unc	Year 2012 Station 378 val	unc	Year 2015 Station 68 val	unc	Year 2020 Station – val	unc	Year 2021 Station 8 val	unc
300	Γ	27	4	28	2	23	2	NaN	NaN	31	2
	Δ	17	7	18	4	17	3	NaN	NaN	19	2
	t_{mode}	10	2	10	1	6	1	NaN	NaN	12	1
500	Γ	NaN	NaN	NaN	NaN	23	2	NaN	NaN	29	1
	D	NaN	NaN	NaN	NaN	16	3	NaN	NaN	17	2
	t_{mode}	NaN	NaN	NaN	NaN	7	1	NaN	NaN	12	1
1000	Γ	NaN	NaN	NaN	NaN	21	3	NaN	NaN	36	2
	D	NaN	NaN	NaN	NaN	21	5	NaN	NaN	28	4
	t_{mode}	NaN	NaN	NaN	NaN	3	1	NaN	NaN	9	1

Table C2. Amundsen Basin

Depth (m)	TTD parameter (years)	2011 Station 218 val	unc	2012 Station – val	unc	2015 Station 81 val	unc	2020 Station – val	unc	2021 Station 16 val	unc	2021 Station 20 val	unc
300	Γ	25	4	NaN	NaN	21	3	NaN	NaN	26	1	NaN	NaN
	Δ	22	8	NaN	NaN	21	6	NaN	NaN	15	2	NaN	NaN
	t_{mode}	5	1	NaN	NaN	3	1	NaN	NaN	11	1	NaN	NaN
500	Γ	NaN	NaN	NaN	NaN	23	3	NaN	NaN	27	2	26	2
	D	NaN	NaN	NaN	NaN	22	6	NaN	NaN	21	3	23	4
	t_{mode}	NaN	NaN	NaN	NaN	4	1	NaN	NaN	7	1	5	1
1000	Γ	NaN	NaN	NaN	NaN	11	3	NaN	NaN	32	2	30	2
	D	NaN	NaN	NaN	NaN	15	7	NaN	NaN	27	4	21	3
	t_{mode}	NaN	NaN	NaN	NaN	1	1	NaN	NaN	7	1	9	1

Table C3. Makarov Basin

Depth (m)	TTD parameter (years)	2011 Station 226 val	unc	2012 Station – val	unc	2015 Station 101 val	unc	2020 Station – val	unc	2021 Station 28 val	unc
300	Γ	23	3	NaN	NaN	22	1	NaN	NaN	30	1
	Δ	9	4	NaN	NaN	11	3	NaN	NaN	16	2
	t_{mode}	15	2	NaN	NaN	11	2	NaN	NaN	14	1
500	Γ	NaN	NaN	NaN	NaN	26	2	NaN	NaN	31	1
	D	NaN	NaN	NaN	NaN	13	3	NaN	NaN	15	2
	t_{mode}	NaN	NaN	NaN	NaN	13	2	NaN	NaN	16	1
1000	Γ	NaN	NaN	NaN	NaN	47	2	NaN	NaN	42	1
	D	NaN	NaN	NaN	NaN	26	2	NaN	NaN	21	2
	t_{mode}	NaN	NaN	NaN	NaN	21	1	NaN	NaN	21	1

Table C4. Canada Basin

Depth (m)	TTD parameter (years)	2011		2012		2015		2020		2021	
	Year										
	Station	–		–		56		CB5		–	
		val	unc	val	unc	val	unc	val	unc	val	unc
500	Γ	NaN	NaN	NaN	NaN	35	1	31	2	NaN	NaN
	D	NaN	NaN	NaN	NaN	9	1	5	2	NaN	NaN
	t_{mode}	NaN	NaN	NaN	NaN	29	0	29	0	NaN	NaN

47

References

Aagaard, K., Swift, J., and Carmack, E.: Thermohaline circulation in the Arctic Mediterranean seas, Journal of Geophysical Research: Oceans, 90, 4833–4846, 1985.

950   Alkire, M. B., Falkner, K. K., Rigor, I., Steele, M., and Morison, J.: The return of Pacific waters to the upper layers of the central Arctic Ocean, Deep Sea Research Part I: Oceanographic Research Papers, 54, 1509–1529, https://doi.org/10.1016/j.dsr.2007.06.004, 2007.

Alkire, M. B., Morison, J., and Andersen, R.: Variability in the meteoric water, sea-ice melt, and Pacific water contributions to the central Arctic Ocean, 2000-2014, Journal of Geophysical Research: Oceans, 120, 1573–1598, https://doi.org/10.1002/2014JC010023, 2015.

Alkire, M. B., Rember, R., and Polyakov, I.: Discrepancy in the Identification of the Atlantic/Pacific Front in the Central Arctic Ocean: NO

955   Versus Nutrient Relationships, Geophysical Research Letters, 46, 3843–3852, https://doi.org/10.1029/2018GL081837, 2019.

Anderson, L., Björk, G., Holby, O., Jones, E., Kattner, G., Koltermann, K., Liljeblad, B., Lindegren, R., Rudels, B., and Swift, J.: Water masses and circulation in the Eurasian Basin: Results from the Oden 91 expedition, Journal of Geophysical Research: Oceans, 99, 3273–3283, 1994.

Anderson, L. G. and Jones, E. P.: Tracing upper waters of the Nansen Basin in the Arctic Ocean, Deep Sea Research Part A. Oceanographic

960   Research Papers, 39, S425–S433, 1992.

Anderson, L. G., Björk, G., Holby, O., Jutterström, S., Mörth, C. M., O'Regan, M., Pearce, C., Semiletov, I., Stranne, C., Stöven, T., Tanhua, T., Ulfsbo, A., and Jakobsson, M.: Shelf–Basin interaction along the East Siberian Sea, Ocean Science, 13, 349–363, https://doi.org/10.5194/os-13-349-2017, 2017.

Bauch, D., Schlosser, P., and Fairbanks, R. G.: Freshwater balance and the sources of deep and bottom waters in the Arctic Ocean inferred

965   from the distribution of H218O, Progress in Oceanography, 35, 53–80, https://doi.org/10.1016/0079-6611(95)00005-2, 1995.

Bauch, D., Van Der Loeff, M. R., Andersen, N., Torres-Valdes, S., Bakker, K., and Abrahamsen, E. P.: Origin of freshwater and polynya water in the Arctic Ocean halocline in summer 2007, Progress in Oceanography, 91, 482–495, https://doi.org/10.1016/j.pocean.2011.07.017, 2011.

Broecker, W. S.: "NO", a conservative water-mass tracer, Earth and Planetary Science Letters, 23, 100–107, https://doi.org/10.1016/0012-

970   821X(74)90036-3, 1974.

Broecker, W. S. and Peng, T.-H.: Tracers in the Sea, Lamont-Doherty Geological Observatory, Columbia University Palisades, New York, 1982.

Casacuberta, N. and Smith, J. N.: Nuclear Reprocessing Tracers Illuminate Flow Features and Connectivity Between the Arctic and Sub-polar North Atlantic Oceans, Annual Review of Marine Science, 15, 203–221, https://doi.org/10.1146/annurev-marine-032122-112413,

975   publisher: Annual Reviews, 2023.

Casacuberta, N., Masqué, P., Henderson, G., Rutgers van-der Loeff, M., Bauch, D., Vockenhuber, C., Daraoui, A., Walther, C., Synal, H.-A., and Christl, M.: First ^{236}U data from the Arctic Ocean and use of ^{236}U/^{238}U and ^{129}I/^{236}U as a new dual tracer, Earth and Planetary Science Letters, 440, 127–134, https://doi.org/10.1016/j.epsl.2016.02.020, 2016.

Casacuberta, N., Christl, M., Vockenhuber, C., Wefing, A.-M., Wacker, L., Masqué, P., Synal, H.-A., and Rutgers van der Loeff, M.: Tracing

980   the Three Atlantic Branches Entering the Arctic Ocean With ^{129}I and ^{236}U, Journal of Geophysical Research: Oceans, 123, 6909–6921, https://doi.org/10.1029/2018JC014168, 2018.

Chamizo, E., Christl, M., López-Lora, M., Casacuberta, N., Wefing, A., and Kenna, T. C.: The Potential of 233U/236U as a Water Mass Tracer in the Arctic Ocean, Journal of Geophysical Research, 127, 12, https://doi.org/10.1029/2021JC017790, 2022.

Chapman, W. L. and Walsh, J. E.: Recent Variations of Sea Ice and Air Temperature in High Latitudes, https://journals.ametsoc.org/view/journals/bams/74/1/1520-0477_1993_074_0033_rvosia_2_0_co_2.xml, section: Bulletin of the American Meteorological Society, 1993.

Christl, M., Vockenhuber, C., Kubik, P., Wacker, L., Lachner, J., Alfimov, V., and Synal, H.-A.: The ETH Zurich AMS facilities: Performance parameters and reference materials, Nuclear Instruments and Methods in Physics Research Section B: Beam Interactions with Materials and Atoms, 294, 29–38, https://doi.org/10.1016/j.nimb.2012.03.004, 2013.

Christl, M., Casacuberta, N., Lachner, J., Maxeiner, S., Vockenhuber, C., Synal, H.-A., Goroncy, I., Herrmann, J., Daraoui, A., Walther, C., and Michel, R.: Status of ^{236}U analyses at ETH Zurich and the distribution of ^{236}U and ^{129}I in the North Sea in 2009, Nuclear Instruments and Methods in Physics Research Section B: Beam Interactions with Materials and Atoms, 361, 510–516, https://doi.org/10.1016/j.nimb.2015.01.005, 2015a.

Christl, M., Casacuberta, N., Vockenhuber, C., Elsässer, C., Bailly du Bois, P., Herrmann, J., and Synal, H.-A.: Reconstruction of the ^{236}U input function for the Northeast Atlantic Ocean: Implications for ^{129}I/^{236}U and ^{236}U/^{238}U-based tracer ages, Journal of Geophysical Research: Oceans, 120, 7282–7299, https://doi.org/10.1002/2015JC011116, 2015b.

Christl, M., Gautschi, P., Maxeiner, S., Müller, A. M., Vockenhuber, C., and Synal, H.-A.: 236U analyses with the ETH Zurich MILEA prototype system, Nuclear Instruments and Methods in Physics Research Section B: Beam Interactions with Materials and Atoms, 534, 61–71, https://doi.org/10.1016/j.nimb.2022.11.009, 2023.

Coachman, L. and Barnes, C.: The contribution of Bering Sea water to the Arctic Ocean, Arctic, 14, 147–161, 1961.

Cooper, L. W., Hong, G. H., Beasley, T. M., and Grebmeier, J. M.: Iodine-129 concentrations in marginal seas of the North Pacific and Pacific-influenced waters of the Arctic Ocean, Marine pollution bulletin, 42, 1347–1356, 2001.

Crameri, F.: Scientific colour maps, https://doi.org/10.5281/zenodo.8409685, 2023.

Dale, D., Christl, M., Vockenhuber, C., Macrander, A., Ólafsdóttir, S., Middag, R., and Casacuberta, N.: Tracing Ocean Circulation and Mixing From the Arctic to the Subpolar North Atlantic Using the ^{129}I–^{236}U Dual Tracer, Journal of Geophysical Research: Oceans, 129, e2024JC021211, https://doi.org/10.1029/2024JC021211, 2024.

Edmonds, H.: Nuclear Fuel Reprocessing And Related Discharges, in: Encyclopedia of Ocean Sciences, pp. 1921–1928, Elsevier, ISBN 978-0-12-227430-5, https://doi.org/10.1006/rwos.2001.0169, 2001.

Gascard, J.-C., Raisbeck, G., Sequeira, S., Yiou, F., and Mork, K. A.: The Norwegian Atlantic Current in the Lofoten basin inferred from hydrological and tracer data (^{129}I) and its interaction with the Norwegian Coastal Current, Geophysical Research Letters, 31, https://doi.org/10.1029/2003GL018303, 2004.

GEBCO Compilation Group, .: GEBCO 2024 Grid, https://doi.org/10.5285/1c44ce99-0a0d-5f4f-e063-7086abc0ea0f, 2024.

Gerke, L., Arck, Y., and Tanhua, T.: Temporal Variability of Ventilation in the Eurasian Arctic Ocean, Journal of Geophysical Research: Oceans, 129, e2023JC020608, https://doi.org/10.1029/2023JC020608, 2024.

Haine, T. W. N. and Hall, T. M.: A Generalized Transport Theory: Water-Mass Composition and Age, Journal of Physical Oceanography, 32, 1932–1946, https://doi.org/10.1175/1520-0485(2002)032<1932:AGTTWM>2.0.CO;2, 2002.

Heuzé, C., Karam, S., Muchowski, J., Padilla, A., Stranne, C., Gerke, L., Tanhua, T., Ulfsbo, A., Laber, C., and Stedmon, C. A.: Physical Oceanography during ODEN expedition SO21 for the Synoptic Arctic Survey, https://doi.org/10.1594/PANGAEA.951266, 2022a.

Heuzé, C., Karam, S., Muchowski, J., Padilla, A., Stranne, C., Gerke, L., Tanhua, T., Ulfsbo, A., Laber, C., and Stedmon, C. A.: Physical Oceanography measured on bottle water samples during ODEN expedition SO21 for the Synoptic Arctic Survey, https://doi.org/10.1594/PANGAEA.951264, 2022b.

50

Jones, E. P. and Anderson, L. G.: On the origin of the chemical properties of the Arctic Ocean halocline, Journal of Geophysical Research, 91, 10759, https://doi.org/10.1029/JC091iC09p10759, 1986.

Jones, E. P., Anderson, L. G., and Swift, J. H.: Distribution of Atlantic and Pacific waters in the upper Arctic Ocean: Implications for circulation, Geophysical Research Letters, 25, 765–768, https://doi.org/10.1029/98GL00464, 1998.

1025 Karcher, M., Smith, J. N., Kauker, F., Gerdes, R., and Smethie, W. M.: Recent changes in Arctic Ocean circulation revealed by iodine-129 observations and modeling, Journal of Geophysical Research: Oceans, 117, n/a–n/a, https://doi.org/10.1029/2011JC007513, 2012.

Khatiwala, S., Tanhua, T., Mikaloff Fletcher, S., Gerber, M., Doney, S., Graven, H. D., Gruber, N., McKinley, G., Murata, A., Rios, A., and Sabine, C. L.: Global ocean storage of anthropogenic carbon, Biogeosciences, 10, 2169–2191, https://doi.org/10.5194/bg-10-2169-2013, 2013.

1030 Kohlbach, D., Fransson, A., Amargant-Arumi, M., Assmann, K. M., Assmy, P., Bratbak, G., Chierici, M., Cristea, A., Divine, D. V., Down, E., Eikrem, W., Foss, \., Gardner, J., Gradinger, R. R., Granskog, M. A., Hess, S., Ingvaldsen, R. B., Koenig, Z., Kwaśniewski, S., Majaneva, S., Marquardt, M., Müller, O., Ntniou, I. V., Ormańczyk, M., Raffel, B., Renaud, P., Renner, A. H. H., De Freitas, T. R., Sen, A., Smoła, Z., Svensen, C., Vader, A., Våge, S., Wiktor, J., Wold, A., Zabłocka, M., Ziegler, A., and Bluhm, B. A.: Nansen and Amundsen basins: Gradients of physico-chemical properties and biota composition with implications for future resource management of the central Arctic
1035 Ocean, Elem Sci Anth, 13, 00016, https://doi.org/10.1525/elementa.2024.00016, 2025.

Korhonen, M., Rudels, B., Marnela, M., Wisotzki, A., and Zhao, J.: Time and space variability of freshwater content, heat content and seasonal ice melt in the Arctic Ocean from 1991 to 2011, Ocean Science, 9, 1015–1055, https://doi.org/10.5194/os-9-1015-2013, 2013.

Kwok, R.: Arctic sea ice thickness, volume, and multiyear ice coverage: losses and coupled variability (1958–2018), Environmental Research Letters, 13, 105005, iSBN: 1748-9326 Publisher: IOP Publishing, 2018.

1040 Körtke, W., Walter, M., Huhn, O., Kanzow, T., and Rhein, M.: Decadal Changes in the Pathways of the Atlantic Water Core in the Arctic Ocean Inferred From Transient Tracers, Journal of Geophysical Research: Oceans, 129, e2024JC021419, https://doi.org/10.1029/2024JC021419, 2024.

Lauvset, S. K., Lange, N., Tanhua, T., Bittig, H. C., Olsen, A., Kozyr, A., Álvarez, M., Azetsu-Scott, K., Brown, P. J., Carter, B. R., Cotrim Da Cunha, L., Hoppema, M., Humphreys, M. P., Ishii, M., Jeansson, E., Murata, A., Müller, J. D., Pérez, F. F., Schirnick, C., Steinfeldt,
1045 R., Suzuki, T., Ulfsbo, A., Velo, A., Woosley, R. J., and Key, R. M.: The annual update GLODAPv2.2023: the global interior ocean biogeochemical data product, Earth System Science Data, 16, 2047–2072, https://doi.org/10.5194/essd-16-2047-2024, 2024.

Le Bras, I., Straneo, F., Muilwijk, M., Smedsrud, L. H., Li, F., Lozier, M. S., and Holliday, N. P.: How Much Arctic Fresh Water Participates in the Subpolar Overturning Circulation?, Journal of Physical Oceanography, 51, 955–973, https://doi.org/10.1175/JPO-D-20-0240.1, 2021.

Marnela, M., Rudels, B., Olsson, K. A., Anderson, L. G., Jeansson, E., Torres, D. J., Messias, M.-J., Swift, J. H., and Watson, A. J.:
1050 Transports of Nordic Seas water masses and excess SF6 through Fram Strait to the Arctic Ocean, Progress in Oceanography, 78, 1–11, https://doi.org/10.1016/j.pocean.2007.06.004, 2008.

McLaughlin, F. A., Carmack, E. C., Macdonald, R. W., and Bishop, J. K. B.: Physical and geochemical properties across the Atlantic/Pacific water mass front in the southern Canadian Basin, Journal of Geophysical Research: Oceans, 101, 1183–1197, https://doi.org/10.1029/95JC02634, _eprint: https://agupubs.onlinelibrary.wiley.com/doi/pdf/10.1029/95JC02634, 1996.

1055 Morison, J., Kwok, R., Peralta-Ferriz, C., Alkire, M., Rigor, I., Andersen, R., and Steele, M.: Changing Arctic Ocean freshwater pathways, Nature, 481, 66–70, https://doi.org/10.1038/nature10705, 2012.

Morison, J., Kwok, R., Dickinson, S., Andersen, R., Peralta-Ferriz, C., Morison, D., Rigor, I., Dewey, S., and Guthrie, J.: The Cyclonic Mode of Arctic Ocean Circulation, Journal of Physical Oceanography, 51, 1053–1075, https://doi.org/10.1175/JPO-D-20-0190.1, 2021.

Newton, R., Schlosser, P., Mortlock, R., Swift, J., and MacDonald, R.: Canadian Basin freshwater sources and changes: Results from the 2005 Arctic Ocean Section, Journal of Geophysical Research: Oceans, 118, 2133–2154, https://doi.org/10.1002/jgrc.20101, 2013.

Paffrath, R., Laukert, G., Bauch, D., Rutgers van der Loeff, M., and Pahnke, K.: Separating individual contributions of major Siberian rivers in the Transpolar Drift of the Arctic Ocean, Scientific Reports, 11, 8216, https://doi.org/10.1038/s41598-021-86948-y, tex.ids= paffrathSeparatingIndividualContributions2021a, 2021.

Pasqualini, A., Schlosser, P., Newton, R., Smethie Jr, W. M., and Friedrich, R.: A Multi-Decade Tracer Study of the Circulation and Spreading Rates of Atlantic Water in the Arctic Ocean, Journal of Geophysical Research: Oceans, 129, https://doi.org/10.1029/2023JC020738, 2024.

Payne, A., Wefing, M., Christl, M., Vockenhuber, C., Williams, W., Smith, J. N., and Casacuberta, N.: Circulation Timescales and Pathways of Atlantic Water in the Canada Basin: Insights From Transient Tracers 129I and 236U, Journal of Geophysical Research, 2024.

Polyakov, I. V., Beszczynska, A., Carmack, E. C., Dmitrenko, I. A., Fahrbach, E., Frolov, I. E., Gerdes, R., Hansen, E., Holfort, J., Ivanov, V. V., Johnson, M. A., Karcher, M., Kauker, F., Morison, J., Orvik, K. A., Schauer, U., Simmons, H. L., Skagseth, \., Sokolov, V. T., Steele, M., Timokhov, L. A., Walsh, D., and Walsh, J. E.: One more step toward a warmer Arctic, Geophysical Research Letters, 32, https://doi.org/10.1029/2005GL023740, 2005.

Polyakov, I. V., Pnyushkov, A. V., Alkire, M. B., Ashik, I. M., Baumann, T. M., Carmack, E. C., Goszczko, I., Guthrie, J., Ivanov, V. V., Kanzow, T., Krishfield, R., Kwok, R., Sundfjord, A., Morison, J., Rember, R., and Yulin, A.: Greater role for Atlantic inflows on sea-ice loss in the Eurasian Basin of the Arctic Ocean, Science, 356, 285–291, https://doi.org/10.1126/science.aai8204, 2017.

Polyakov, I. V., Rippeth, T. P., Fer, I., Alkire, M. B., Baumann, T. M., Carmack, E. C., Ingvaldsen, R., Ivanov, V. V., Janout, M., Lind, S., Padman, L., Pnyushkov, A. V., and Rember, R.: Weakening of Cold Halocline Layer Exposes Sea Ice to Oceanic Heat in the Eastern Arctic Ocean, Journal of Climate, 33, 8107–8123, https://doi.org/10.1175/JCLI-D-19-0976.1, 2020.

Polyakov, I. V., Ingvaldsen, R. B., Pnyushkov, A. V., Bhatt, U. S., Francis, J. A., Janout, M., Kwok, R., and Skagseth, \.: Fluctuating Atlantic inflows modulate Arctic atlantification, Science, 381, 972–979, https://doi.org/10.1126/science.adh5158, 2023.

Polyakov, I. V., Pnyushkov, A. V., Charette, M., Cho, K.-H., Jung, J., Kipp, L., Muilwijk, M., Whitmore, L., Yang, E. J., and Yoo, J.: Atlantification advances into the Amerasian Basin of the Arctic Ocean, Science Advances, 11, eadq7580, https://doi.org/10.1126/sciadv.adq7580, 2025.

Proshutinsky, A., Dukhovskoy, D., Timmermans, M.-L., Krishfield, R., and Bamber, J. L.: Arctic circulation regimes, Philosophical Transactions of the Royal Society A: Mathematical, Physical and Engineering Sciences, 373, 20140 160, https://doi.org/10.1098/rsta.2014.0160, 2015.

Pérez-Tribouillier, H., Jaccard, S. L., Blaser, P., Christl, M., Creac'h, L., Hölemann, J., Scheiwiller, M., Vockenhuber, C., Wefing, A. M., and Casacuberta, N.: The Role of the St. Anna Trough in Atlantic Water Transport Into the Arctic Ocean: A Novel Radiogenic Isotope Assessment Using Iodine, Uranium, and Neodymium, Journal of Geophysical Research: Oceans, 130, e2024JC022 050, https://doi.org/10.1029/2024JC022050, publisher: John Wiley & Sons, Ltd, 2025.

Raimondi, L., Tanhua, T., Azetsu-Scott, K., Yashayaev, I., and Wallace, D.: A 30 -Year Time Series of Transient Tracer-Based Estimates of Anthropogenic Carbon in the Central Labrador Sea, Journal of Geophysical Research: Oceans, 126, https://doi.org/10.1029/2020JC017092, 2021.

Raimondi, L., Wefing, A., and Casacuberta, N.: Anthropogenic Carbon in the Arctic Ocean: Perspectives From Different Transient Tracers, Journal of Geophysical Research: Oceans, 129, e2023JC019 999, https://doi.org/10.1029/2023JC019999, 2024.

Rantanen, M., Karpechko, A. Y., Lipponen, A., Nordling, K., Hyvärinen, O., Ruosteenoja, K., Vihma, T., and Laaksonen, A.: The Arctic has warmed nearly four times faster than the globe since 1979, Communications Earth & Environment, 3, 168, https://doi.org/10.1038/s43247-022-00498-3, 2022.

Rudels, B.: Arctic Ocean circulation, processes and water masses: A description of observations and ideas with focus on the period prior to the International Polar Year 2007–2009, Progress in Oceanography, 132, 22–67, https://doi.org/10.1016/j.pocean.2013.11.006, 2015.

Rudels, B., Anderson, L. G., and Jones, E. P.: Formation and evolution of the surface mixed layer and halocline of the Arctic Ocean, Journal of Geophysical Research: Oceans, 101, 8807–8821, https://doi.org/10.1029/96JC00143, 1996.

Rudels, B., Jones, E. P., Schauer, U., and Eriksson, P.: Atlantic sources of the Arctic Ocean surface and halocline waters, Polar Research, 23, 181–208, https://doi.org/10.3402/polar.v23i2.6278, 2004.

Sakaguchi, A., Kawai, K., Steier, P., Quinto, F., Mino, K., Tomita, J., Hoshi, M., Whitehead, N., and Yamamoto, M.: First results on 236U levels in global fallout, Science of the Total Environment, 407, 4238–4242, 2009.

Schauer, U., Loeng, H., Rudels, B., Ozhigin, V. K., and Dieck, W.: Atlantic Water flow through the Barents and Kara Seas, Deep Sea Research Part I: Oceanographic Research Papers, 49, 2281–2298, https://doi.org/10.1016/S0967-0637(02)00125-5, 2002.

Schulz, K., Koenig, Z., Muilwijk, M., Bauch, D., Hoppe, C. J. M., Droste, E. S., Hoppmann, M., Chamberlain, E. J., Laukert, G., Stanton, T., Quintanilla-Zurita, A., Fer, I., Heuzé, C., Karam, S., Mieruch-Schnülle, S., Baumann, T. M., Vredenborg, M., Tippenhauer, S., and Granskog, M. A.: The Eurasian Arctic Ocean along the MOSAiC drift in 2019–2020: An interdisciplinary perspective on physical properties and processes, Elem Sci Anth, 12, 00114, https://doi.org/10.1525/elementa.2023.00114, 2024.

Serreze, M. C., Barrett, A. P., Stroeve, J. C., Kindig, D. N., and Holland, M. M.: The emergence of surface-based Arctic amplification, The Cryosphere, 3, 11–19, https://doi.org/10.5194/tc-3-11-2009, publisher: Copernicus GmbH, 2009.

Smethie, W. M., Fine, R. A., Putzka, A., and Jones, E. P.: Tracing the flow of North Atlantic Deep Water using chlorofluorocarbons, Journal of Geophysical Research: Oceans, 105, 14 297–14 323, https://doi.org/10.1029/1999JC900274, 2000.

Smith, J. N., McLaughlin, F. A., Smethie, W. M., Moran, S. B., and Lepore, K.: Iodine-129, ^{137}Cs, and CFC-11 tracer transit time distributions in the Arctic Ocean, Journal of Geophysical Research, 116, https://doi.org/10.1029/2010JC006471, 2011.

Smith, J. N., Karcher, M., Casacuberta, N., Williams, W. J., Kenna, T., and Smethie, W. M.: A Changing Arctic Ocean: How Measured and Modeled [129]I Distributions Indicate Fundamental Shifts in Circulation Between 1994 and 2015, Journal of Geophysical Research: Oceans, 126, https://doi.org/10.1029/2020JC016740, 2021.

Smith, J. N., Smethie, W. M., and Casacuberta, N.: Synoptic [129]I and CFC–SF$_6$ Transit Time Distribution (TTD) Sections Across the Central Arctic Ocean From the 2015 GEOTRACES Cruises, Journal of Geophysical Research: Oceans, 127, https://doi.org/10.1029/2021JC018120, 2022.

Snoeijs-Leijonmalm, P., , and the SAS-Oden 2021 Scientific Party: Expedition Report SWEDARCTIC Synoptic Arctic Survey 2021 with icebreaker Oden, Tech. rep., Swedish Polar Research Secretariat, 2022.

Stöven, T. and Tanhua, T.: Ventilation of the Mediterranean Sea constrained by multiple transient tracer measurements, Ocean Science, 10, 439–457, https://doi.org/10.5194/os-10-439-2014, 2014.

Stöven, T., Tanhua, T., Hoppema, M., and Bullister, J. L.: Perspectives of transient tracer applications and limiting cases, Ocean Science, 11, 699–718, https://doi.org/10.5194/os-11-699-2015, 2015.

Stöven, T., Tanhua, T., Hoppema, M., and von Appen, W.-J.: Transient tracer distributions in the Fram Strait in 2012 and inferred anthropogenic carbon content and transport, Ocean Science, 12, 319–333, https://doi.org/10.5194/os-12-319-2016, 2016.

Sumata, H., De Steur, L., Divine, D. V., Granskog, M. A., and Gerland, S.: Regime shift in Arctic Ocean sea ice thickness, Nature, 615, 443–449, https://doi.org/10.1038/s41586-022-05686-x, 2023.

Tanhua, T., Jones, E. P., Jeansson, E., Jutterström, S., Smethie, W. M., Wallace, D. W. R., and Anderson, L. G.: Ventilation of the Arctic Ocean: Mean ages and inventories of anthropogenic CO_2 and CFC-11, Journal of Geophysical Research, 114, https://doi.org/10.1029/2008JC004868, 2009.

Thyng, K., Greene, C., Hetland, R., Zimmerle, H., and DiMarco, S.: True Colors of Oceanography: Guidelines for Effective and Accurate Colormap Selection, Oceanography, 29, 9–13, https://doi.org/10.5670/oceanog.2016.66, 2016.

Timmermans, M.-L. and Toole, J. M.: The Arctic Ocean's Beaufort Gyre, Annual Review of Marine Science, 15, 223–248, https://doi.org/10.1146/annurev-marine-032122-012034, 2023.

Vockenhuber, C., Casacuberta, N., Christl, M., and Synal, H.-A.: Accelerator Mass Spectrometry of ^{129}I towards its lower limits, Nuclear Instruments and Methods in Physics Research Section B: Beam Interactions with Materials and Atoms, 361, 445–449, https://doi.org/10.1016/j.nimb.2015.01.061, 2015.

Wang, Q., Shu, Q., and Wang, F.: Recent emergence of Arctic atlantification dominated by climate warming, Science Advances, 10, eadq5235, https://doi.org/10.1126/sciadv.adq5235, 2024.

Waugh, D. W., Hall, T. M., and Haine, T. W. N.: Relationships among tracer ages, Journal of Geophysical Research, 108, https://doi.org/10.1029/2002JC001325, 2003.

Waugh, D. W., Hall, T. M., Mcneil, B. I., Key, R., and Matear, R. J.: Anthropogenic CO_2 in the oceans estimated using transit time distributions, Tellus B: Chemical and Physical Meteorology, 58, 376–389, https://doi.org/10.1111/j.1600-0889.2006.00222.x, 2006.

Wefing, A.-M.: I-129 and U-236 data from the ODEN expedition SO21 for the Synoptic Arctic Survey, https://doi.org/10.5281/zenodo.15056897, 2025.

Wefing, A.-M., Casacuberta, N., Christl, M., Gruber, N., and Smith, J. N.: Circulation timescales of Atlantic Water in the Arctic Ocean determined from anthropogenic radionuclides, Ocean Science, 17, 111–129, https://doi.org/10.5194/os-17-111-2021, 2021.

Wefing, A.-M., Casacuberta, N., Christl, M., and Dodd, P. A.: Water mass composition in Fram Strait determined from the combination of 129I and 236U: Changes between 2016, 2018, and 2019, Frontiers in Marine Science, p. 16, https://doi.org/10.3389/fmars.2022.973507, 2022.

Whitmore, L. M., Pasqualini, A., Newton, R., and Shiller, A. M.: Gallium: A New Tracer of Pacific Water in the Arctic Ocean, Journal of Geophysical Research: Oceans, 125, https://doi.org/10.1029/2019JC015842, 2020.

Östlund, H. G. and Hut, G.: Arctic Ocean water mass balance from isotope data, Journal of Geophysical Research, 89, 6373, https://doi.org/10.1029/JC089iC04p06373, rEAD, 1984.